Article

Immunity

CD163^{+} red pulp macrophages interact with marginal metallophilic macrophages during blood-stage malaria to maintain splenic architecture

Graphical abstract

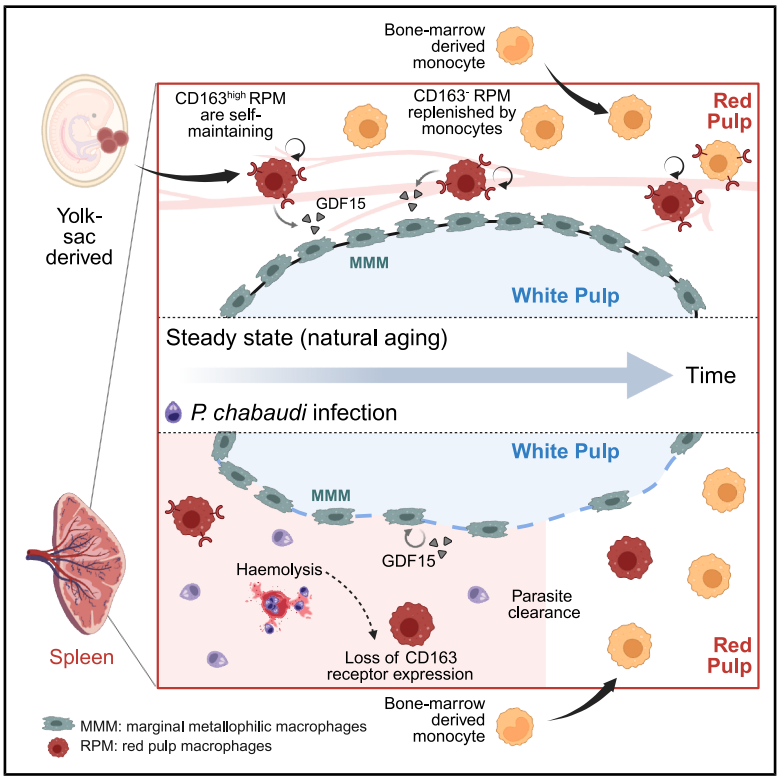

Highlights

- CD163 distinguishes transcriptionally and functionally distinct RPM populations
- CD163^{high} RPMs exhibit specialized iron-recycling and stress-response programs
- RPM^{iron} cells promote MMM recovery through GDF15-dependent signaling
- Distinct macrophage subsets display differential ontogeny and infection dynamics

Authors

Katharina Mauel, Daria Hirschmann, Nelli Blank-Stein, ..., William R. Heath, Lynette Beattie, Elvira Mass

Correspondence

lynette.beattie@unimelb.edu.au (L.B.), elvira.mass@uni-bonn.de (E.M.)

In brief

Splenic macrophages adapt to malaria through subset-specific remodeling and inter-macrophage communication. Using fate mapping, single-cell transcriptomics, and genetic perturbation, Mauel et al. show that red pulp macrophages (RPMs) and marginal metallophilic macrophages (MMMs) are predominantly yolk sac derived. They identify a CD163^{high} iron-recycling RPM subset that is lost after malaria and find that stress response factor GDF15-dependent signaling supports MMM maintenance.

Mauel et al., 2026, Immunity *59*, 1–19
October 13, 2026
https://doi.org/10.1016/j.immuni.2026.07.006

CellPress

Immunity

CellPress
OPEN ACCESS

Article

CD163+ red pulp macrophages interact with marginal metallophilic macrophages during blood-stage malaria to maintain splenic architecture

Katharina Mauel,[1,2] Daria Hirschmann,[1,2] Nelli Blank-Stein,[1] Marie-Louise Diefenbach-Wilke,[1] Theresa Eulgem,[1] Shirley Le,[2] Samuel N. Breit,[3] Miguel P. Soares,[4] Vicky Wang-Wei Tsai,[3] Florent Ginhoux,[5,6,7,8] William R. Heath,[2] Lynette Beattie,[2,9,*] and Elvira Mass[1,9,10,*]

[1]Developmental Biology of the Immune System, Life & Medical Sciences (LIMES) Institute, University of Bonn 53115 Bonn, Germany
[2]Department of Microbiology and Immunology (DMI), Peter Doherty Institute (PDI), Melbourne, VIC 3000, Australia
[3]Cytokine Biology and Inflammation Research Program, St Vincent's Center of Applied Medical Research (AMR), University of New South Wales, Sydney, NSW 2010, Australia
[4]Gulbenkian Institute for Molecular Medicine, 1649-028 Lisboa, Portugal
[5]INSERM U1015, Gustave Roussy Cancer Campus, Villejuif 94800, France
[6]Shanghai Institute of Immunology, Department of Immunology and Microbiology, Shanghai Jiao Tong University School of Medicine, Shanghai 200025, China
[7]Singapore Immunology Network, Agency for Science, Technology and Research, Singapore 138648, Singapore
[8]Translational Immunology Institute, SingHealth Duke-NUS Academic Medical Centre, Singapore 169856, Singapore
[9]These authors contributed equally
[10]Lead contact
*Correspondence: lynette.beattie@unimelb.edu.au (L.B.), elvira.mass@uni-bonn.de (E.M.)
https://doi.org/10.1016/j.immuni.2026.07.006

SUMMARY

The spleen harbors distinct macrophage subsets that support circulatory homeostasis and initiate immune responses, but the ontogeny and long-term dynamics of these populations remain incompletely understood. Here, we identified a transcriptionally and developmentally distinct CD163-expressing red pulp macrophage (CD163^{high} RPM) population that arose from yolk sac progenitors and occupied a vascular-associated niche. Using fate-mapping models, we showed that CD163^{-} RPMs were progressively replenished by monocytes during aging, whereas CD163^{high} RPMs were mainly self-maintaining. During blood-stage malaria, CD163^{high} RPMs were rapidly depleted, failed to recover despite parasite clearance, and were replaced by CD163^{-} monocyte-derived RPMs. Single-cell RNA sequencing and genetic mouse models revealed that CD163 deficiency exacerbated structural disintegration of the marginal zone and selectively impaired marginal metallophilic macrophage (MMM) recovery, underscoring a CD163-dependent RPM-MMM crosstalk. This study reveals that the sustained loss of a specialized, yolk sac-derived CD163^{high} RPM subset rewires splenic architecture and inter-macrophage crosstalk long after malaria resolution.

INTRODUCTION

The spleen maintains circulatory homeostasis by filtering the blood and eliminating senescent red blood cells (RBCs) and blood-borne pathogens. It consists of lymphocyte-rich white pulp and the red pulp with its characteristic open circulation, enabling direct interactions with circulating cells and rapid immune responses.[1] Splenic macrophages mediate homeostatic and immunological functions through four major subsets, each occupying a distinct anatomical niche[1,2]: white pulp macrophages (WPMs), which clear apoptotic lymphocytes[3]; marginal zone macrophages (MZMs) and marginal metallophilic macrophages (MMMs), both dependent on the nuclear receptor Lxrα and involved in antigen uptake, processing, and transfer[4]; and red pulp macrophages (RPMs), characterized by high F4/80 expression and essential for erythrophagocytosis and iron recycling.[5,6] These subsets are shaped by local cues and transcriptional regulators, such as *Spic* for RPMs.[7] Under steady-state conditions, RPMs recycle iron from damaged/senescent RBCs in a Spi-C-dependent manner.[8] These erythrophagocytic macrophages rely on the heme oxygenase-1 (Hmox1/HO-1)[9] for heme degradation and ferroportin (SLC40A1)[10] for iron export[7,8] and support erythropoiesis.[11]

Macrophage function has been proposed to be tightly linked to developmental origin, a concept advanced through fate-mapping models.[12–14] During adulthood almost all myeloid cells are derived from hematopoietic stem cells (HSCs), with the exception of certain tissue-resident mast cells[15] and macrophages.[16–18] These macrophages originate from yolk sac-derived erythro-myeloid progenitors (EMPs), populate the

Please cite this article in press as: Mauel et al., CD163+ red pulp macrophages interact with marginal metallophilic macrophages during blood-stage malaria to maintain splenic architecture, Immunity (2026), https://doi.org/10.1016/j.immuni.2026.07.006

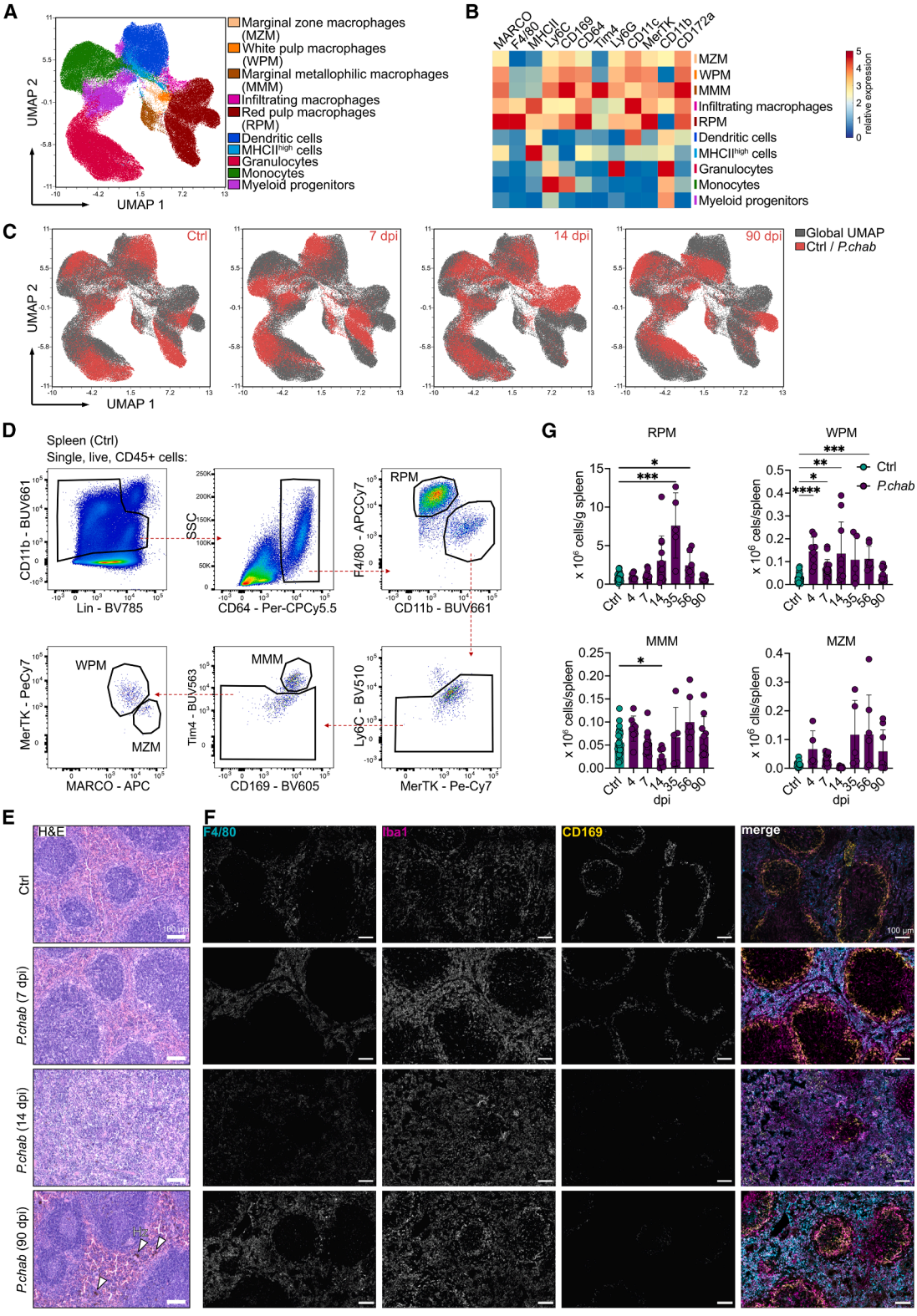

Figure 1. *P. chabaudi* infection transiently remodels splenic macrophage populations and architecture

(A) OMIQ-based clustering of CD45+, CD11b+, and MHC class II+ splenocytes from Ctrl and 7, 14, and 90 dpi mice based on marker expression in (B).

(B) Expression of characteristic myeloid markers across clusters.

(C) UMAP overlay of Ctrl, 7, 14, and 90 dpi samples.

(legend continued on next page)

Please cite this article in press as: Mauel et al., CD163+ red pulp macrophages interact with marginal metallophilic macrophages during blood-stage malaria to maintain splenic architecture, Immunity (2026), https://doi.org/10.1016/j.immuni.2026.07.006

embryo before the onset of definitive hematopoiesis[19,20] and can self-maintain in some tissues throughout life, with varying contribution of HSC-derived cells.[12,20,21] Although some splenic macrophages emerge postnatally,[6,22] the ontogeny and longevity of splenic macrophage subsets remain incompletely understood.

Beyond homeostasis, macrophages of both EMP and HSC origin support pathogen clearance.[21] Monocyte-derived macrophages are recruited during acute infections and are often characterized by a more pro-inflammatory phenotype, whereas resident macrophages support the resolution phase.[23,24] During malaria, a life-threatening hemolytic disease caused by *Plasmodium* infection, the complex life-cycle of the parasite[25,26] complicates vaccine development.[27] After the asymptomatic liver-stage, merozoites are released into the circulation and invade RBCs,[27] which circulate through the spleen and can be eliminated by resident macrophages.[28] High parasite burdens during the acute phase of the infection require recruitment of innate immune cells to achieve a protective immune-mediated inflammatory response.[29] Parasite-induced rupture of RBCs (intravascular hemolysis) can lead to anemia and depletion of splenic erythrophagocytic macrophages. This releases hemoglobin and labile heme, which has high redox activity, aggravating malaria severity.[30] To restrain oxidative damage, scavengers like haptoglobin form a complex with labile heme,[31] which binds to the CD163 receptor, expressed on erythrophagocytic macrophages. Internalization facilitates heme catabolism via Hmox1 and iron recycling.[32] Thus, splenic macrophages contribute to early containment of blood-borne infections, but their subset-specific roles, replacement dynamics, crosstalk, and long-term recovery remain unresolved.

Using fate-mapping models, we resolve the developmental origins and cellular dynamics of splenic macrophage subsets during homeostasis and malaria, uncovering a CD163-based heterogeneity of RPMs. We show that blood-stage malaria induces a selective and irreversible loss of embryonic CD163^{high} RPMs, partly driven by heme stress. Single-cell RNA sequencing (scRNA-seq) and macrophage-specific knockout (KO) models reveal a critical crosstalk between CD163^{high} RPMs and MMMs required to preserve splenic architecture and function at steady state and during infection.

RESULTS

Malaria transiently disrupts splenic architecture and macrophage composition

To assess splenic macrophage responses to blood-stage malaria, we analyzed CD11b$^+$/MHC class II$^+$ myeloid cells at acute (7 and 14 days post-infection [dpi]) and chronic (90 dpi) time points following *Plasmodium chabaudi AS* (*P. chabaudi*) infection, a non-lethal experimental model of malaria. We established a flow cytometry panel for simultaneous analysis of RPMs (F4/80^{high} CD11b^{low}), MMMs (CD169$^+$Tim4$^+$), MZMs (Tim4^{int}MARCO$^+$), and WPMs (CD11b$^+$MerTK$^+$) combined with unsupervised clustering and visualization (Figures 1A–1C). Combined uniform manifold approximation and projection (UMAP) analysis of control, acute, and chronic samples confirmed reliable detection of all macrophage subsets based on their characteristic surface markers (Figures 1A and 1B). Monocytes (Ly6C$^+$), granulocytes (Ly6G$^+$), dendritic cells (CD11c$^+$MHC class II$^+$), and myeloid progenitors (CD11b$^+$Ly6C$^+$) were detected in control and infected conditions across all time points. At 14 dpi, we observed a distinct cluster of CD11c^{high} infiltrating macrophages and MHC class II^{high} myeloid cells that upregulated macrophage markers including macrophage receptor with collagenous structure (MARCO) and MER receptor tyrosine kinase (MerTK) (Figures 1B and 1C). While MMMs, MZMs, and WPMs returned to control-like UMAP positions at 90 dpi, RPMs remained persistently shifted (Figure 1C), reflecting sustained surface marker changes. This streamlined panel identified all known splenic macrophage populations (Figure 1D).

We analyzed spleen morphology, weight, and histology 4–90 dpi (Figures 1E and S1A). As expected, parasitemia followed a cyclic course during the first 3–4 weeks and became undetectable from day 56 onward (Figures S1B and S1C). Peak parasitemia coincided with anemia, reflected by reduced RBC counts, hematocrit, and hemoglobin around 14 dpi, alongside increased circulating leukocytes, all of which normalized after the acute phase (>35 dpi) (Figure S1D). Severe splenomegaly developed during peak parasitemia and gradually resolved by 90 dpi (Figure S1E).

H&E staining revealed marginal zone disruption from 14 dpi, followed by immune cell infiltration indicated by splenomegaly (Figures 1E and S1E). Although hemozoin deposits persisted at 90 dpi, splenic architecture had largely normalized (Figure 1E). Using CD169 to detect MMMs, we confirmed transient loss and subsequent regeneration of the marginal zone structure (Figure 1F). While the transient reduction in RPM frequency among CD45$^+$ cells following blood-stage malaria has been described,[5,33] the dynamics of all splenic macrophage subsets during the chronic phase remained unknown. We quantified absolute macrophage numbers per spleen and per gram of tissue, respectively (Figures 1G and S1F). RPMs expanded during the first month of infection, peaking at 35 dpi, before returning to baseline by 90 dpi. WPMs increased initially in numbers and returned to baseline by 90 dpi. In contrast, MMMs and MZMs declined during the first peak of parasitemia (14 dpi) but gradually recovered (Figures 1G and S1F), consistent with histological observations (Figures 1E and 1F).

To investigate infection-induced emergency myelopoiesis that may replenish splenic macrophages via circulating monocytes,[34] we quantified bone marrow (BM) hematopoietic stem

(D) Gating strategy for RPMs, MMMs, WPMs, and MZMs.
(E and F) Representative H&E staining (E) and immunofluorescent images (F) of spleens from Ctrl and *P. chab*-infected mice (7, 14, and 90 dpi). Scale bar, 100 μm. Representative for n = 2–3, 2 independent experiments.
(G) Quantification of macrophages in Ctrl and *P. chab* -infected mice (4–90 dpi) by flow cytometry. n (Ctrl) > 20, n (*P. chab*) = 5–15 per time point, 2–3 independent experiments, Kruskal-Wallis test, *$p < 0.05$, **$p < 0.01$, ***$p < 0.001$, and ****$p < 0.0001$. Bars represent mean ± SD; individual mice are represented as circles. MMMs, marginal metallophilic macrophages; MZMs, marginal zone macrophages, RPMs, red pulp macrophages, WPMs, white pulp macrophages; and dpi: days post-infection.
See also Figures S1 and S2.

Please cite this article in press as: Mauel et al., CD163+ red pulp macrophages interact with marginal metallophilic macrophages during blood-stage malaria to maintain splenic architecture, Immunity (2026), https://doi.org/10.1016/j.immuni.2026.07.006

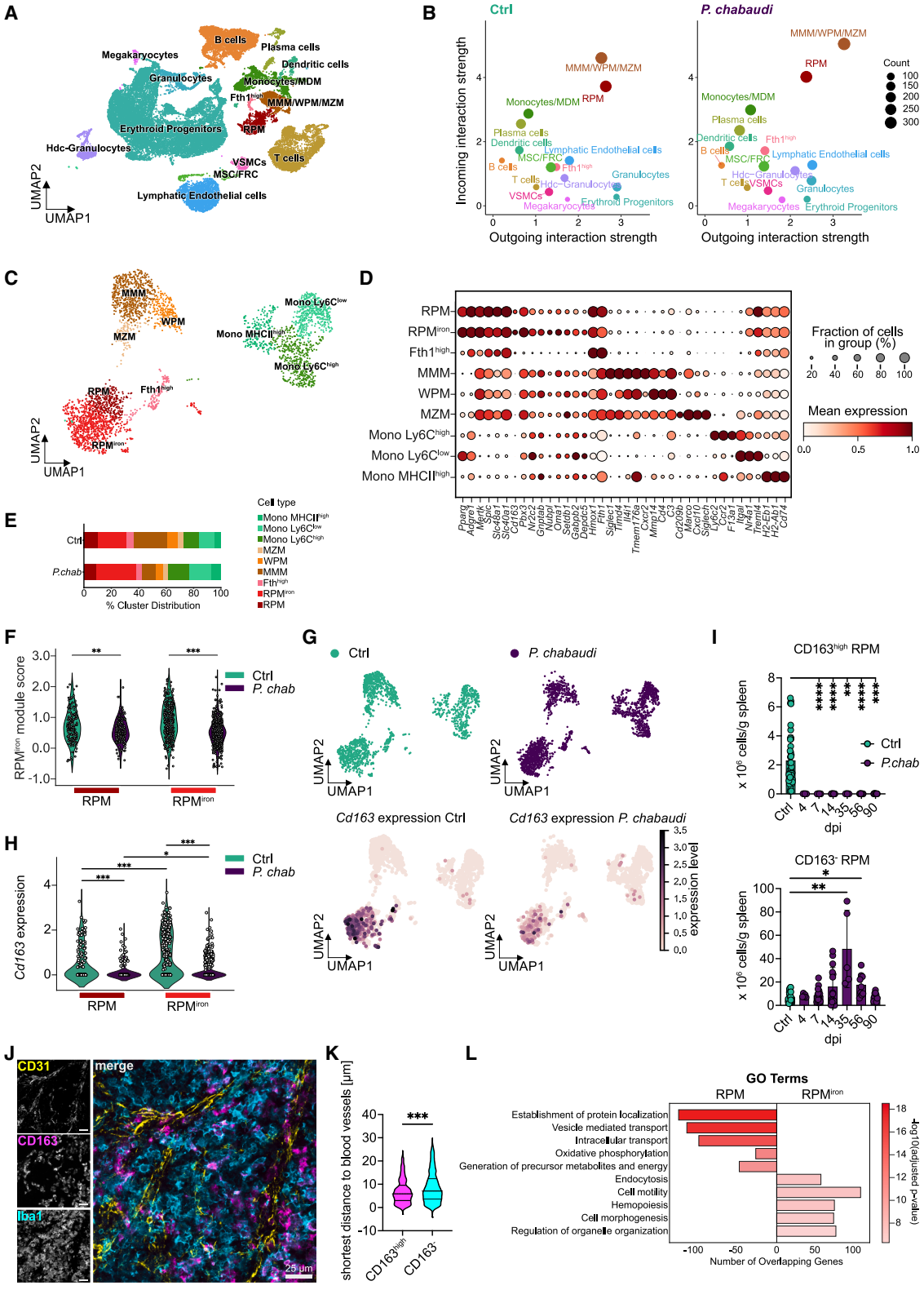

Figure 2. A CD163-expressing RPM subset localizes to the vasculature and is lost after malaria

(A) scRNA-seq of Ctrl and *P. chab*-infected splenocytes visualized by UMAP.

(B) Incoming and outgoing interaction strength of identified cell clusters determined by CellChat.

(C) UMAP visualization of RPM, MMM/WPM/MZM, Fth1^{high}, and monocyte/MDM subclusters.

(legend continued on next page)

Please cite this article in press as: Mauel et al., CD163+ red pulp macrophages interact with marginal metallophilic macrophages during blood-stage malaria to maintain splenic architecture, Immunity (2026), https://doi.org/10.1016/j.immuni.2026.07.006

and progenitor cells (HSPCs) and peripheral blood immune cells 4–90 dpi. Conventional gating of HSPC populations (Figure S2A) revealed that long-term-HSCs and multipotent progenitor 4 (MPP4) were unaffected by infection (Figure S2B). Short-term-HSCs and granulocyte-monocyte-progenitors increased at 56 dpi. In contrast, MPP2 and MMP3 populations were transiently elevated, peaking at 7 dpi and returning to baseline by 14 dpi (Figure S2B), indicating a temporary emergency myelopoietic response.

We next analyzed the systemic cell output into blood, including B and T lymphocytes, granulocytes, and monocyte subsets (Figures S2C and S2D). While most populations remained stable, we observed a decrease of B cells 7–14 and a specific increase in MHC class II^{+} monocytes (Figure S2D), potentially contributing to the influx of MHC class II^{+} myeloid cells during this period (Figures 1A–1C).

Together, peak parasitemia coincided with splenic architectural disruption, RPM expansion, transient BM progenitor activation, and increased monocytic output, all of which largely returned to homeostasis after parasite clearance.

The CD163-expressing RPM population is lost after malaria infection

Although the spleen appeared morphologically regenerated at 90 dpi, we hypothesized that malaria induced long-lasting molecular changes within splenic macrophage populations, particularly in RPMs, as suggested by their altered UMAP distribution (Figure 1C). To determine persistent transcriptional changes, we sequenced fluorescence-activated cell sorting (FACS)-enriched CD64^{+} and MACS-enriched CD45^{-} cells from control and 90 dpi animals (Figures 2A and S3A–S3D). Analysis of all scRNA-seq conditions revealed distinct myeloid clusters, including RPMs (defined by high *Adgre1*, *Mrc1*, and *Adam22* expression), a combined cluster of marginal zone and white pulp macrophages (MMMs, MZMs, and WPMs; expressing *Marco*, *Siglec1*, and *Timd4*), a Fth1^{high} macrophage population enriched for ferritin h chain 1 (*Fth1*), and a monocyte/monocyte-derived macrophage (MDM) cluster characterized by *Ly6c2*, *Ccr2*, and low *Adgre1* expression (Figure S3D; Table S1). In addition to macrophages, other immune cell types (granulocytes, dendritic cells, B cells, and T cells) and non-immune stromal cells (lymphatic endothelial cells, vascular smooth muscle cells [VSMCs], and a mixed mesenchymal cluster [mesenchymal stem cell/ fibroblastic reticular cell (MSC/FRC)]) were also detected (Figures 2A and S3D).

To infer intercellular communication networks, we applied CellChat analysis. Both interaction number and overall interaction strength were elevated at 90 dpi compared to controls (Figures S3E and S3F). RPMs exhibited the highest interaction strength (Figure S3F), suggesting that they function as dominant communication hubs after infection. Outgoing versus incoming interaction strength analysis further confirmed that macrophage subsets maintained central roles in spleen-wide communication under both homeostatic and post-infection conditions. However, signaling activity was markedly enhanced post-malaria, especially among MMM/WPM/MZM subsets (Figure 2B), indicating persistent reorganization of communication networks.

To define long-lasting transcriptional changes within splenic macrophages, we subclustered all macrophages from the scRNA-seq dataset. In addition to expected populations (RPMs, MMMs, MZMs, WPMs, MHC class II^{high} macrophages, and monocytes), we identified two transcriptionally distinct macrophage subsets: Fth1^{high} macrophages marked by high expression of *Fth1 and Hmox1*, and a second RPM cluster that had significantly higher expression of iron metabolism-related genes (*Cd163*[35,36] and *Setdb1*[37]), hereafter referred to as RPM^{iron} (Figures 2C and 2D; Table S2). This heterogeneity has not been previously described, where CD163 surface expression was thought to be broadly shared among all RPMs.[6,38] While proportion-based analyses suggested altered macrophage composition after infection, including reduced MMM abundance (Figure 2E), these analyses did not reflect absolute population dynamics (Figures 1G and S1F). We therefore focused on the RPM^{iron} population during homeostasis and post-malaria recovery.

To identify iron-related genes associated with RPM^{iron}, we performed marker gene analysis of genes co-expressed with *Cd163* (Figure S3G). *Hmox1*, *Slc40a1*, *Stab2*, and *Tfrc*, genes involved in iron uptake, recycling, and transport,[39] were integrated into a module score-based analysis, revealing persistent changes in coordinated iron-related transcriptional programs after infection, with the strongest changes in RPM^{iron} cells (Figures 2F and S3H). Feature and split-UMAP representations showed *Cd163* expression in both RPM and RPM^{iron} populations, with higher expression in RPM^{iron}, reduced *Cd163*

(D) Cluster-specific marker genes shown in (C).
(E) Relative distribution of macrophage clusters in Ctrl and *P. chab* infection.
(F) Module score analysis of iron-related genes (*Hmox1*, *Slc40a1*, *Stab2*, and *Tfrc*) in RPM and RPM^{iron}. Mann-Whitney test, followed by Benjamini-Hochberg false discovery rate (FDR) correction, $^{**}p < 0.01$ and $^{***}p < 0.001$.
(G) UMAP of macrophage subclusters showing *Cd163* expression in Ctrl to *P. chab* infection.
(H) *Cd163* expression in RPMs and RPM^{iron} in Ctrl to *P. chab* infection. Mann-Whitney test with two-sided comparison, $^{*}p < 0.05$, $^{**}p < 0.01$, and $^{***}p < 0.001$. Cells from $n = 2$ biological replicates per condition. Circles represent single cells.
(I) Quantification of CD163^{-} and CD163^{high} RPMs in Ctrl and *P. chab*-infected mice (1–90 dpi) by flow cytometry. n (Ctrl) > 20, n (*P.chab*) = 5–20 per time point, 2–4 independent experiments, Kruskal-Wallis test, $^{*}p < 0.05$, $^{**}p < 0.01$, $^{***}p < 0.001$, and $^{****}p < 0.0001$. Bars represent mean ± SD; individual mice are represented as circles.
(J) Representative immunofluorescence image showing localization of CD163^{high} RPMs relative to CD31^{+} vasculature during steady state. Scale bar, 25 μm. Representative for $n = 2$.
(K) Distance of CD163^{high} and CD163^{-} RPMs to CD31^{+} blood vessels. 4 spleens, n (CD163^{high}) = 305 cells, n (CD163^{-}) = 657 cells, Mann-Whitney test, $^{***}p<0.001$.
(L) GO terms enriched in RPM^{iron} versus RPMs.
FRCs, fibroblastic reticular cells; MSCs, mesenchymal stem cells; VSMCs, vascular smooth muscle cells.
See also Figures S3 and S4.

Please cite this article in press as: Mauel et al., CD163+ red pulp macrophages interact with marginal metallophilic macrophages during blood-stage malaria to maintain splenic architecture, Immunity (2026), https://doi.org/10.1016/j.immuni.2026.07.006

transcript abundance 90 dpi, and differences in the relative positioning of RPM^{iron} cells within the UMAP embedding (Figure 2G). Quantification of normalized gene expression confirmed higher *Cd163* expression in RPM^{iron} than conventional RPMs and a global reduction in *Cd163* expression after malaria (Figure 2H). To examine this at the protein level, we performed flow cytometry and immunofluorescence during acute and chronic infection. CD163 protein was expressed by a subset of RPMs under steady-state conditions, hereafter referred to as CD163^{high} RPMs to distinguish the protein-defined population, and these cells progressively declined in number from 4 dpi, with loss persisting through 180 dpi (Figures 2I and S4A–S4D). Immunofluorescence analysis showed that CD163^{high} RPMs localized significantly closer to CD31^{+} blood vessels than CD163^{-} RPMs, consistent with a vascular-associated niche (Figures 2J and 2K).

To assess functional differences between RPM^{iron} and conventional RPMs, we performed Gene Ontology (GO) enrichment analysis on differentially expressed genes (DEGs) under steady-state conditions. RPMs were enriched for pathways involved in vesicle-mediated transport, oxidative phosphorylation, and protein localization, indicative of active metabolic and homeostatic functions. In contrast, RPM^{iron} showed enrichment in gene programs associated with immune activation, cell motility, and organelle regulation (Figure 2L; Table S3), suggesting a more responsive or migratory phenotype. Despite persistent *Cd163* transcript expression after infection (Figures 2G and 2H), RPM^{iron} failed to fully re-express CD163 protein (Figure 2I), suggesting that the sustained reduction of CD163^{high} RPMs after malaria may result from both the loss of these cells and incomplete re-expression of CD163 in remaining cells.

Fate mapping reveals distinct developmental trajectories of RPM populations

To investigate the ontogeny of CD163^{high} and CD163^{-} RPMs during steady state and after infection, we used the *Cxcr4*^{CreERT2}*; Rosa26*$^{LSL\text{-}tdTomato}$ fate-mapping model (Figure S5A), which labels BM-derived monocytes after tamoxifen injection of adult mice.[14,40] After five daily tamoxifen injections and a 4-week washout period prior to infection, we observed ~90% tdTomato labeling of circulating monocytes in both control and *P. chabaudi*-infected mice across all time points (Figure S5B). In control mice, CD163^{high} RPMs showed only ~10% tdTomato labeling up to 56 days after the washout period. This increased modestly to ~30% by 90 days (i.e. 4 months post-tamoxifen), indicating that CD163^{high} RPMs are largely independent of monocyte influx under steady-state conditions. Also in this model, CD163^{high} RPMs were undetectable early after *P. chabaudi* infection. CD163^{-} RPMs initially showed ~18% tdTomato labeling, which increased to >45% 4 months after tamoxifen injection (90 dpi) (Figure S5B), suggesting that CD163^{-} RPM constitute a distinct subset with greater monocyte input over time. Following infection, CD163^{-} RPM reached ~80% tdTomato labeling by 14 dpi and ~85% at 90 dpi (Figure S5B), indicating monocyte replenishment of most RPMs after infection. Together, these findings suggest that the adult RPM compartment is heterogeneous: CD163^{-} RPMs are replaced by monocytes over time, whereas CD163^{high} RPMs are largely self-maintaining under homeostatic conditions and only slowly replenished.

Splenic macrophage subsets are differentially replenished by monocytes after malaria

While previous studies proposed that RPMs are predominantly yolk sac-derived,[16,41] our fate-mapping data indicated a notable contribution of BM-derived cells to the adult RPM pool, especially in the CD163^{-} population. To dissect both the developmental origin and long-term persistence of splenic macrophages, we employed the *Tnfrsf11a*^{Cre}*; Rosa26*$^{LSL\text{-}YFP}$*; Ms4a3*^{FlpO}*; Rosa26*$^{FSF\text{-}tdTomato\ 43}$ double fate-mapping model, which simultaneously traces yolk sac-derived pre-macrophages (pMacs, via yellow fluorescent protein [YFP]) and BM-derived monocytes (via tdTomato) (Figure 3A). Efficient labeling of pMacs and their progeny in *Tnfrsf11a*^{Cre}*; Rosa26*$^{LSL\text{-}YFP}$ mice has been previously demonstrated, but because *Tnfrsf11a*, a core macrophage gene, is also expressed in monocytes once they differentiate into tissue-resident macrophages, we integrated the *Ms4a3*^{FlpO} driver to selectively mark monocyte-derived cells.[42] This dual labeling approach enables identification of both cellular origin and monocyte-derived cells that acquired tissue residency, as evidenced by co-expression of YFP and tdTomato (Figures 3A and S5C).

We first focused on CD163^{high} RPMs. At 1 week of age, prior to the full segregation of red and white pulp evidenced by the random distribution of CD169, YFP^{+} CD163^{high} cells were detectable in the parenchyma (Figure S5D). Comparing developmental trajectories of CD163^{high} and CD163^{-} RPMs in fetal, early postnatal, and young adult mice using flow cytometry, both RPM subpopulations were almost exclusively yolk sac-derived until 2 months of age (Figures 3B–3D) when splenic architecture was fully developed, and YFP^{+} CD163^{high} cells were evenly distributed throughout the red pulp, with minimal overlap with tdTomato^{+} cells (Figure S5E). During aging (3–12 months), the developmental trajectories diverged slightly: ~60% CD163^{high} RPMs remained of yolk sac origin (Figure 3B), while CD163^{-} RPMs were gradually replaced by long-lived monocyte-derived cells, with >50% YFP^{+}tdTomato^{+} by 1 year of age (Figure 3C).

Given the distinct ontogeny of RPM subsets, we examined their replacement following *P. chabaudi* infection. In both control and infected mice, Ly6C^{+} and MHC class II^{+} blood monocytes were almost uniformly tdTomato^{+} and lacked YFP, confirming their BM origin (Figures S5F and S5G). This absence of YFP^{+} single-positive monocytes validated YFP expression as a specific marker for yolk sac-derived macrophages. Approximately 15%–20% of circulating monocytes co-expressed tdTomato and YFP, potentially reflecting monocytes already primed toward tissue residency. In control spleens, F4/80^{+} RPMs predominantly expressed YFP, with minimal tdTomato, consistent with a largely yolk sac-derived tissue-resident macrophage population (Figure 3E). CD163^{high} RPMs maintained their YFP^{+} signature throughout (7–90 dpi) in uninfected mice, confirming their yolk sac origin under homeostatic conditions (Figure S5H). Upon *P. chabaudi* infection, yolk sac-derived (YFP^{+}) CD163^{-} RPMs sharply declined, troughing at 14 dpi (Figure 3E). At this time, a transient tdTomato^{+} RPM population emerged (12.5% ± 9%) that lacked YFP expression, representing recently recruited monocyte-derived macrophages that had not yet upregulated *Tnfrsf11a*. By 35 dpi, most CD163^{-} RPMs were double labeled (YFP^{+}tdTomato^{+}), indicating differentiation into long-lived macrophages that either once or now stably expressed *Tnfrsf11a* (Figure 3E). In contrast, CD163^{high} RPMs remained undetectable

Please cite this article in press as: Mauel et al., CD163+ red pulp macrophages interact with marginal metallophilic macrophages during blood-stage malaria to maintain splenic architecture, Immunity (2026), https://doi.org/10.1016/j.immuni.2026.07.006

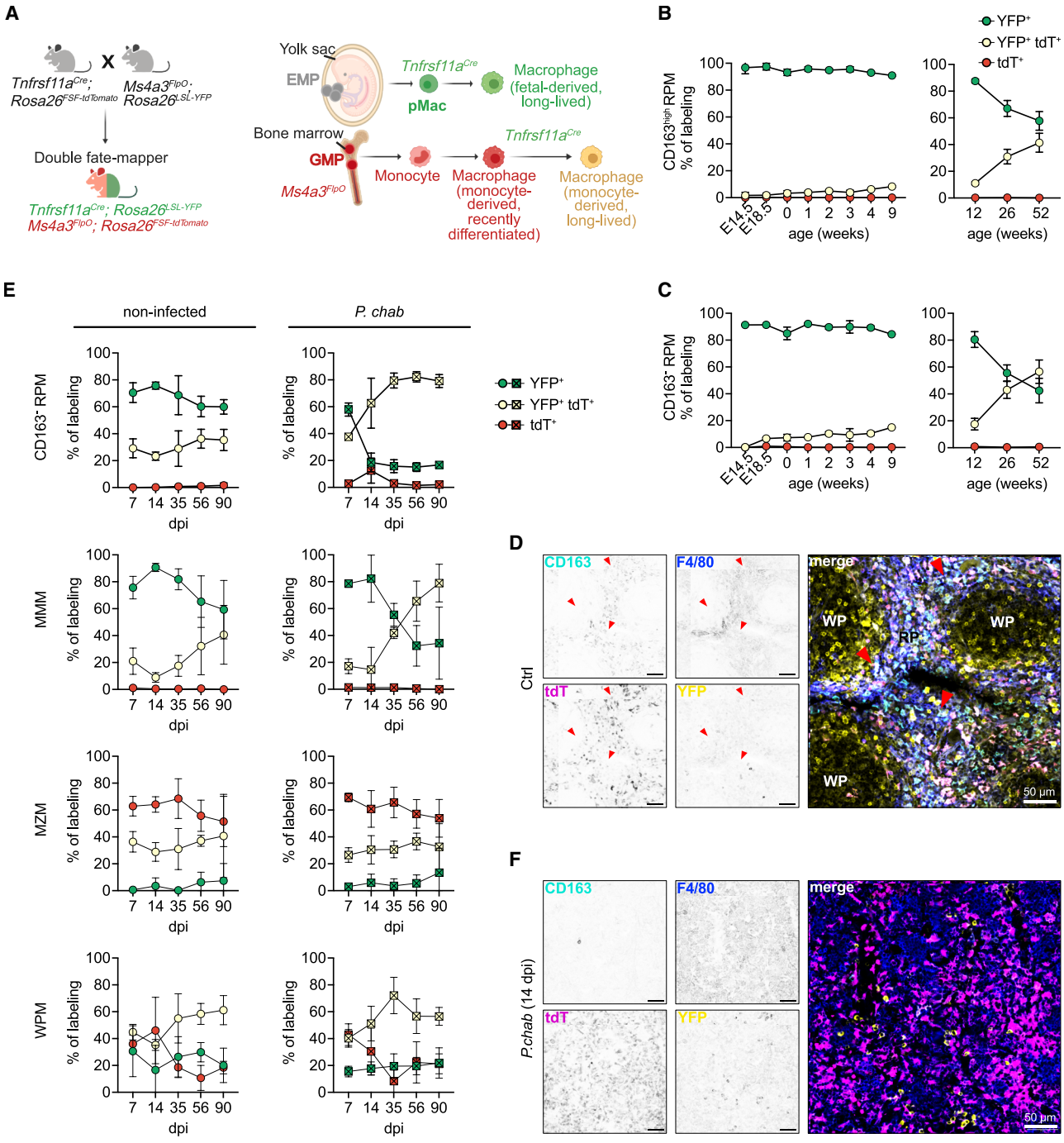

Figure 3. Splenic macrophage subsets follow distinct developmental trajectories that diverge after malaria

(A) Breeding scheme of *Tnfrsf11a*^{Cre}; *Rosa26*$^{LSL\text{-}YFP}$; *Ms4a3*^{FlpO}; and *Rosa26*$^{FSF\text{-}tdTomato}$ mice and schematic of macrophage lineage tracing. Generated with Biorender.

(B and C) Labeling efficiency in CD163^{high} (B) and CD163^{-} RPMs (C) in young (E14.5 and 18.5, n = 3, 1 experiment; weeks 1–9, n = 4–9, 2 independent experiments) and aged mice (n = 7–12, 3 independent experiments). Circles represent mean ± SD.

(D) Representative immunofluorescence image of splenic red pulp (RP) and white pulp (WP) in steady state. Arrows indicate co-expression of CD163 with F4/80 and YFP in CD163^{high} RPMs. Scale bar, 50 µm. Representative for n = 5, 5 independent experiments.

(E) Labeling efficiency of CD163^{-} RPM (n = 3–7 per time point, 2–3 independent experiments), MMM, MZM, and WPM (n = 3–5 per time point, 2 independent experiments) in Ctrl and *P. chab*-infected mice. Circles (Ctrl) and squares (*P.chab*) represent mean ± SD.

(F) Representative immunofluorescence image showing disruption of splenic architecture and loss of CD163 signal at 14 dpi with *P. chab*. Scale bar, 50 µm. Representative for n = 3, 2 independent experiments.

See also Figure S5.

Please cite this article in press as: Mauel et al., CD163+ red pulp macrophages interact with marginal metallophilic macrophages during blood-stage malaria to maintain splenic architecture, Immunity (2026), https://doi.org/10.1016/j.immuni.2026.07.006

throughout infection, suggesting that this population does not regenerate after inflammatory challenge (not shown and Figures 2G and 3F). This remodeling was paralleled by profound structural changes in the spleen. At 14 dpi, the red pulp was dominated by F4/80+tdTomato+ macrophages, and the marginal zone was no longer discernible (Figure 3F), reflecting a collapse of splenic architecture during acute infection.

The breakdown of marginal zone organization prompted us to investigate the fate of MZMs, MMMs, and WPMs, all of which contribute to maintaining splenic architecture and function. Previous studies suggested that MZMs and MMMs are predominantly HSC-derived,[6,43] while WPMs are presumed to originate mainly from postnatal monocytes because the white pulp forms only a few weeks after birth.[38] Our double fate-mapper challenged this view and revealed a more complex picture. Under steady-state conditions, MMMs were predominantly yolk sac-derived (YFP+), whereas MZMs showed frequent replacement by BM-derived monocytes (Figure 3E). Upon *P. chabaudi* infection, yolk sac-derived MMMs progressively declined between 14 and 56 dpi, with infiltrating monocytes differentiating into long-lived MMMs. By 90 dpi, >60% of MMMs were YFP+tdTomato+, indicating stable integration as long-lived monocyte-derived cells. In contrast, WPMs displayed heterogeneity. At steady state, ~20%–30% of WPMs were YFP+, indicating a yolk sac origin. A second fraction (20%–40%) consisted of tdTomato+ cells, reflecting recently arrived monocytes that had not yet upregulated *Tnfrsf11a*. The largest proportion (~50%) was double labeled (YFP+tdTomato+), suggesting these are long-lived, tissue-resident macrophages of monocyte origin (Figure 3E).

Taken together, the double fate-mapping model revealed that splenic macrophages follow distinct developmental trajectories, with CD163^{high} RPMs being yolk sac-derived and largely self-maintaining, while CD163^{-} RPMs, MMMs, and a subset of WPMs were progressively replenished by monocyte-derived cells. WPMs exhibited heterogeneity, consisting of yolk sac-derived cells, short-lived monocytes, and a dominant population of long-lived, monocyte-derived tissue-resident macrophages.

Loss of CD163 expression on macrophages is a hallmark of malaria

Having observed a pronounced loss of CD163^{high} RPMs during *P. chabaudi* infection, we next asked whether this was a generalizable feature of malaria. To address this, we infected mice with *P. yoelii NL* and *P. berghei ANKA* and analyzed spleens at 7 dpi, when CD163^{high} RPMs were already absent in *P. chabaudi* infection. Mice infected with either *P. yoelii* or *P. berghei* developed typical pathology, including splenomegaly (Figure S6A) and parasitemia (Figure S6B). Both infections caused a reduction in CD163^{-} RPMs and a complete loss of CD163^{high} RPMs at 7 dpi (Figure S6C), confirmed by immunofluorescence, while the overall splenic architecture, including CD169+ MMMs lining the marginal zone, remained preserved (Figure S6D).

Given that our scRNA-seq data showed persistence of the transcriptional CD163^{iron} RPM cluster, corresponding to CD163^{high} RPMs, we hypothesized that receptor shedding rather than cell loss may occur. However, circulating CD163 concentrations were also reduced at 7 dpi compared with uninfected controls (Figure S6E), arguing against continuous receptor shedding as the primary mechanism. To study the kinetics of CD163 loss, we performed a time-course analysis during *P. chabaudi* and *P. yoelii* infection, revealing a transient increase in circulating CD163 peaking at 2 dpi in both models, followed by a decline and significantly reduced concentrations from 7 dpi (Figures S6F and S6G).

Next, we assessed RPM dynamics during *P. yoelii* infection, a model lacking recrudescent infection. Parasitemia peaked around 14 dpi (Figure S6H), and the overall CD163^{-} RPM pool declined during the first week of infection (Figure S6I). A wave of monocyte recruitment at 4 dpi was followed by gradual replenishment of the CD163^{-} RPM pool by 7 dpi. Despite this recovery, CD163^{high} RPMs remained undetectable long-term, mirroring the findings in *P. chabaudi* infection (Figures S6I and S6J).

To test if loss of CD163 expression was specific to malaria or a more general feature of inflammation, we examined viral and bacterial infection models. In lymphocytic choriomeningitis virus (LCMV)-infected mice, CD163^{high} RPMs were significantly reduced during the first week and did not recover to control levels even 140 dpi. In contrast, CD163^{-} RPMs initially increased at 7 dpi, before returning to baseline 42 dpi (Figure S6K). A similar pattern was observed following systemic lipopolysaccharide (LPS) injection. CD163^{high} RPMs were significantly reduced by 2 dpi, and CD163^{-} RPMs also diminished by 4 dpi (Figure S6L), coinciding with peak splenomegaly (Figure S6M). However, in the LPS model, all RPMs, including CD163^{high} cells, partially recovered by 56 dpi (Figure S6L).

Together, these findings suggested that loss of CD163 expression was a robust and conserved response to malaria, irrespective of the parasite species. In contrast, virus- and bacteria-induced inflammation transiently reduced but did not abolish CD163^{high} RPMs, highlighting pathogen-specific differences in macrophage responses.

Persistent loss of CD163^{high} RPMs is linked to hemolysis

Having observed a complete and sustained loss of CD163^{high} RPMs following blood-stage malaria, unlike the partial loss and recovery seen in viral and bacterial infections, we next asked whether ongoing parasite presence was required to prevent their regeneration. Treatment of *P. chabaudi*-infected mice with chloroquine after the first two peaks of parasitemia, which reliably eliminated parasites (Figures S7A and S7B), did not rescue CD163^{high} RPMs, which remained undetectable in the spleen 90 dpi, whereas the CD163^{-} RPM population returned to control levels (Figure S7C).

This finding suggested that the absence of CD163 expression was not directly linked to chronic parasite infection. We therefore interrogated the CD163 pathway more mechanistically. CD163 binds hemoglobin-haptoglobin complexes, internalizes them for lysosomal degradation and iron recycling, and is then recycled to the cell surface (Figure S7D). Given this link to iron/heme metabolism, we quantified splenic iron content upon infection. At 14 dpi, iron content was drastically reduced compared with steady-state conditions (Figure S7E), consistent with previous descriptions.[5] Prussian blue staining revealed a profound iron loss in disorganized spleens 14 dpi, whereas iron was distributed throughout the red pulp in uninfected tissue (Figure S7F).

Since malaria is a hemolytic infection, we hypothesized that parasite-induced hemolysis dysregulates iron metabolism, thereby impairing macrophage function[44] and CD163^{high} RPM

Please cite this article in press as: Mauel et al., CD163+ red pulp macrophages interact with marginal metallophilic macrophages during blood-stage malaria to maintain splenic architecture, Immunity (2026), https://doi.org/10.1016/j.immuni.2026.07.006

maintenance. To model hemolysis in the absence of infection, we treated mice with phenylhydrazine, a chemical inducer of intravascular hemolysis, and analyzed splenic RPMs at 7 and 56 days post-treatment (dpt) (Figure S7G). At 7 dpt, CD163^{-} RPMs were elevated while CD163^{high} RPMs were nearly absent (Figure S7H), accompanied by disrupted splenic architecture and decreased iron content, mimicking the acute malaria response (Figure S7I). However, by 56 dpt, both splenic structure and iron distribution, assessed by Prussian blue staining, had normalized, and CD163^{high} RPMs had partially recovered, though not to baseline levels (Figures S7I and S7J).

Together, these data suggested that sustained absence of CD163 expression in RPMs after malaria was not driven by parasite persistence but by infection-induced hemolysis.

CD163 deficiency aggravates splenic disintegration during malaria

Having established that blood-stage malaria leads to a sustained loss of CD163^{high} RPMs, we asked whether the absence of the CD163 receptor itself contributed to impaired splenic recovery. We followed the course of *P. chabaudi* infection in a newly established CD163-deficient mouse line (*Cd163*$^{-/-}$) (Figures S7K and S7L). Successful deletion was confirmed via immunofluorescence (Figure S7M) and associated with the expected reduction in splenic iron stores (Figure S7N). Under steady-state conditions, CD163 deficiency did not impact splenic architecture (Figure 4A), and *Cd163*$^{-/-}$ mice and littermate controls developed comparable splenomegaly and parasitemia upon infection (Figure 4B). Parasitemia at 10 dpi was modestly elevated in wild-type (WT) mice compared with *Cd163*$^{-/-}$ animals, while overall parasite control remained similar between genotypes (Figure 4C), suggesting that CD163 was not essential for parasite control. Quantification of splenic macrophage subsets (RPM, MMM, MZM, and WPM) showed no significant differences in total macrophage numbers between genotypes at steady state (Figure 4D). The KO model precluded discrimination of RPM heterogeneity, therefore only total F4/80^{+} RPMs were assessed. Upon infection, WPM and MZM counts were comparable between *Cd163*$^{-/-}$ mice and littermate controls at 14 and 35 dpi. However, MMMs were significantly reduced in *Cd163*$^{-/-}$ mice 14 dpi compared with controls (Figure 4D). Immunofluorescence showed that infected *Cd163*$^{+/+}$ mice retained a disrupted but discernible marginal zone lined with CD169^{+} MMMs, while *Cd163*$^{-/-}$ mice showed a complete loss of CD169 signal and more extensive architectural disintegration (Figures 4A and 4E). Both genotypes displayed intact marginal zone organization at steady state, suggesting that the absence of CD163 compromises splenic integrity during the acute phase (14 dpi) of malaria. MMMs normalized in number in *Cd163*$^{-/-}$ mice at 35 dpi while exhibiting elevated RPM numbers relative to uninfected *Cd163*$^{-/-}$ mice and infected littermate controls (Figure 4D). These findings suggested that while CD163 was not required for parasite control, its absence during infection transiently disrupted the splenic architecture and MMM homeostasis.

Malaria perturbs Gdf15-dependent RPM-to-MMM trophic signaling

The observed expansion of RPMs in *Cd163*$^{-/-}$ mice during the resolution phase, alongside the transient loss and delayed recovery of MMMs, raised the possibility of compensatory or regulatory interactions between these two macrophage populations. Given that MMM loss was exacerbated in the absence of CD163 expression in RPMs during infection, and that CellChat analysis indicated elevated signaling activity among splenic macrophages, we hypothesized that malaria disrupts a homeostatic communication axis between RPMs and MMMs. To investigate this, we analyzed intercellular signaling networks within macrophage subsets in our scRNA-seq dataset. MMMs showed the highest incoming interaction strength both in control spleens and at 90 dpi with *P. chabaudi* (Figure 5A), suggesting that they function as principal recipients of signals from other macrophage populations.

Pathway-level inference using CellChat showed that certain macrophage-driven homeostatic signals, including a proliferation-inducing ligand (APRIL) and IL-16, were reduced in infected animals, indicating a loss of macrophage-mediated steady-state signaling (Figure 5B). In contrast, angiopoietin-like (ANGPTL), macrophage migration inhibitory factor (MIF), fibroblast growth factor (FGF), and growth arrest-specific (GAS) signaling pathways were generally upregulated post-infection,suggesting a shift toward reparative or remodeling functions. However, analysis at the individual macrophage population level revealed divergent pathway dynamics (Figure 5C). For example, while GALECTIN signaling was broadly upregulated after infection, it was specifically downregulated in RPM^{iron}. Similarly, while most macrophage subsets showed increased CC chemokine ligand (CCL) signaling, MMMs exhibited a reduction in this pathway following infection.

To further dissect the molecular programs underlying altered macrophage responses, we performed DEG analysis across all macrophage subsets. Despite increased overall outgoing signaling from MZMs and WPMs (Figure 5A), the most pronounced changes were detected in RPM^{iron} and RPMs as well as in MMMs (Figure 5D; Table S4), enabling GO overrepresentation analysis (Figure 5E; Table S5). For RPMs, GO enrichment revealed overlapping transcriptional programs in RPM^{iron} and conventional RPMs. Downregulated genes were associated with terms such as synapse organization, regulation of immune response, and cell adhesion, suggesting reduced cell-cell communication and immunoregulatory homeostasis. In contrast, upregulated genes were enriched for antigen processing and presentation of exogenous antigen and cell activation, reflecting enhanced immune surveillance and activation. For MMMs, GO enrichment revealed a distinct transcriptional profile compared with RPMs. Downregulated genes were linked to response to toxic substance, myeloid cell differentiation, and cell chemotaxis, indicating reduced environmental sensing and recruitment functions. In contrast, upregulated genes were associated with translation, ribosome biogenesis, and cellular response to lipopolysaccharide, suggesting a metabolic reprogramming toward biosynthesis and inflammatory readiness. Together, these data indicated fundamentally different long-term adaptations in RPMs and MMMs following *P. chabaudi* infection.

Given the pronounced MMM loss in *Cd163*$^{-/-}$ mice, we inferred ligand-receptor interactions between these macrophage populations. This analysis revealed that signaling pathways involving key growth and survival factors, including *Gdf15*

Please cite this article in press as: Mauel et al., CD163+ red pulp macrophages interact with marginal metallophilic macrophages during blood-stage malaria to maintain splenic architecture, Immunity (2026), https://doi.org/10.1016/j.immuni.2026.07.006

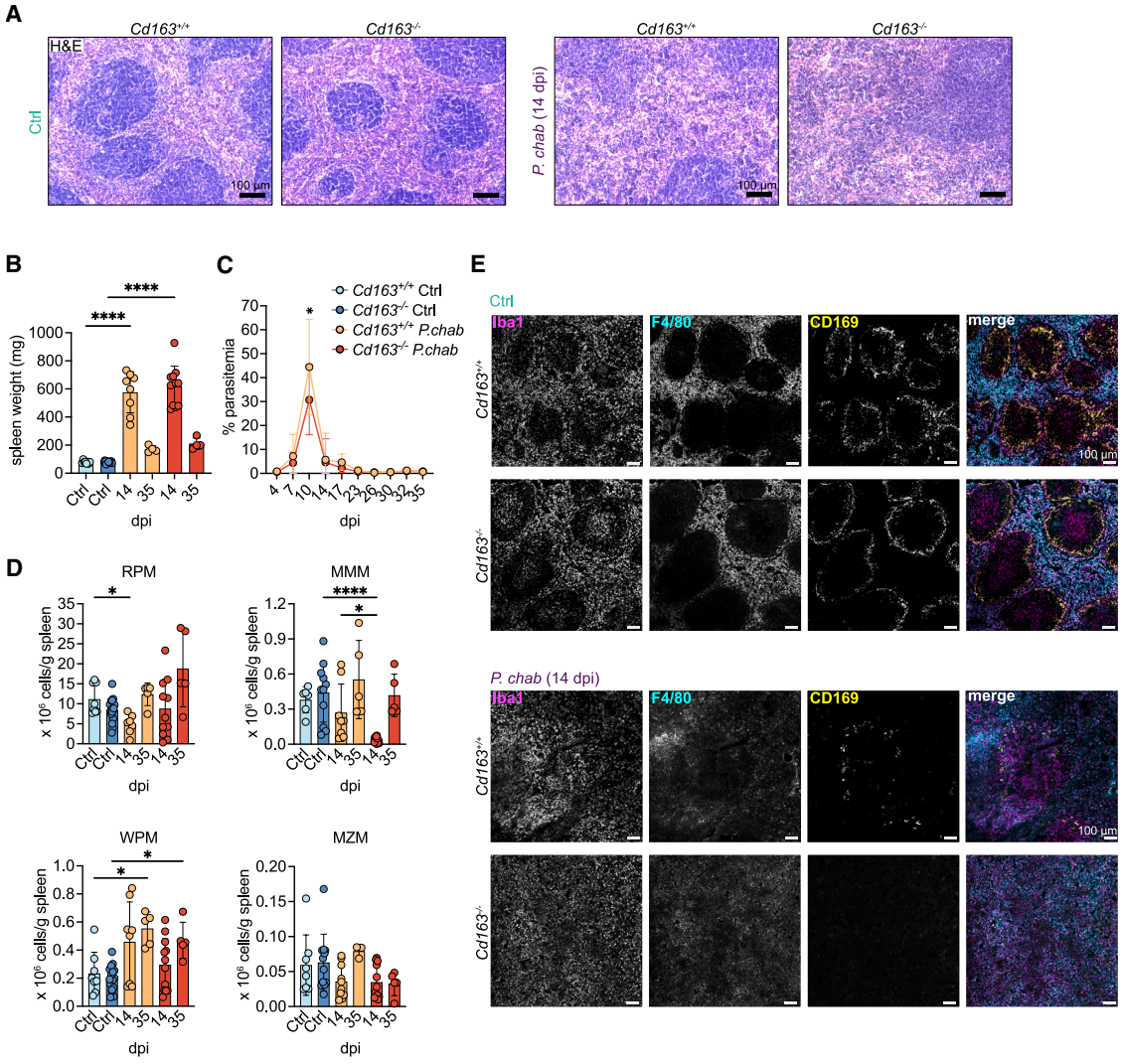

Figure 4. CD163 deficiency aggravates splenic disintegration and impairs MMM recovery during *P. chabaudi* infection

(A) Representative H&E staining of spleens from *Cd163*$^{+/+}$ and *Cd163*$^{-/-}$ mice in Ctrl and 14 dpi with *P. chab*. Scale bar, 100µm. Representative for $n = 3$, 2 independent experiments.

(B) Spleen weights of *Cd163*$^{+/+}$ and *Cd163*$^{-/-}$ in Ctrl (Cd163$^{+/+}$: $n = 7$, *Cd163*$^{-/-}$: $n = 16$) and *P. chab* infection at 14 and 35 dpi (*Cd163*$^{+/+}$: $n = 4$–6, *Cd163*$^{-/-}$: $n = 4$–9). 2–3 independent experiments, one-way ANOVA with multiple comparisons, ****$p < 0.0001$.

(C) Parasitemia in *Cd163*$^{+/+}$ and *Cd163*$^{-/-}$ mice until 35 dpi with *P. chab*. $n = 5$–30, 2–4 independent experiments, Mann-Whitney test, *$p < 0.05$. Circles represent mean ± SD.

(D) Quantification of splenic RPM, MMM, WPM, and MZM of Ctrl (*Cd163*$^{+/+}$ $n = 8$, *Cd163*$^{-/-}$ $n = 12$–16) and *P. chab*-infected mice (*Cd163*$^{+/+}$ $n = 3$–10, *Cd163*$^{-/-}$ $n = 5$–12) at 14 and 35 dpi by flow cytometry. 2–3 independent experiments, Kruskal-Wallis test, *$p < 0.05$, and ****$p < 0.0001$.

(E) Representative immunofluorescence images of spleens from *Cd163*$^{+/+}$ and *Cd163*$^{-/-}$ mice in Ctrl and 14 dpi with *P. chab*. Scale bar, 100 µm. Representative for $n = 2$, 2 independent experiments. In (B) and (D), bars represent mean ± SD; individual mice are represented as circles.

See also Figures S6 and S7.

(expressed by both RPM^{iron} and RPMs) and *Igf1* (restricted to RPM^{iron}), were significantly reduced in RPMs at 90 dpi, with MMMs identified as primary recipients of these signals via *Tgfbr2* and *Igf1r*, respectively (Figure 6A). Likewise, *Lgals9*, contributing to signals via *Tgfbr2* and *Igf1r*, was downregulated in RPM^{iron} following infection. This consistent loss of trophic signaling from RPMs to MMMs suggested that RPM^{iron} serve as a critical source of niche-supporting signals required for MMM maintenance in homeostasis. At 90 dpi, MMMs upregulated *Gdf15*, *Igf1*, and *Lgals9*, which are normally supplied by RPM^{iron}, suggesting a compensatory attempt to sustain their own survival in the absence of sufficient external input. Analysis of normalized gene expression confirmed significant downregulation of *Gdf15*, *Igf1*, and *Lgals9* in RPM^{iron} and concomitant upregulation in MMMs following infection (Figure 6B). Similarly, *Gdf15* was significantly reduced in RPMs, reinforcing the notion of impaired inter-macrophage signaling. Indeed, macrophages were the main source of *Gdf15* and *Igf1*, with expression

Please cite this article in press as: Mauel et al., CD163+ red pulp macrophages interact with marginal metallophilic macrophages during blood-stage malaria to maintain splenic architecture, Immunity (2026), https://doi.org/10.1016/j.immuni.2026.07.006

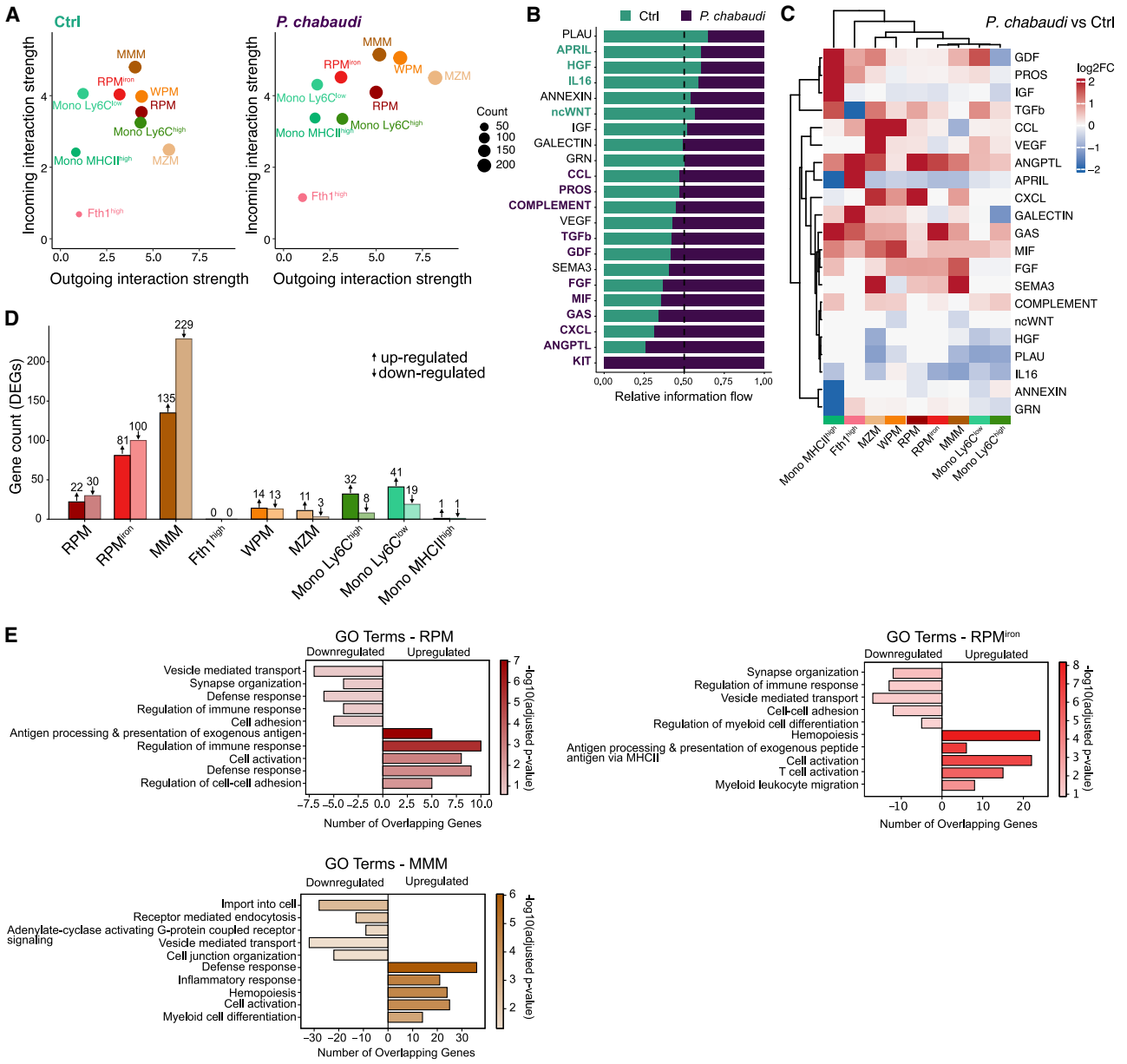

Figure 5. Malaria reprograms intercellular signaling and transcriptional programs across splenic macrophages

(A) Visualization of incoming and outgoing interaction strength of macrophage clusters in Ctrl and *P. chab* infection determined by CellChat.

(B) CellChat analysis of intercellular communication networks among splenic macrophages in Ctrl to *P. chab* infection. Pathways enriched in Ctrl highlighted in cyan; pathways enriched in *P. chab* highlighted in purple.

(C) CellChat analysis of pathways differentially regulated between Ctrl and *P. chab* infection across splenic macrophage subsets.

(D) DEGs (adjusted *p* value: 0.05, log2FC: 0.25) across splenic macrophage populations and monocytes.

(E) GO overrepresentation analysis visualizing up- or downregulated pathways in RPM^{iron}, RPMs, and MMMs.

absent in monocytes and stromal cells, whereas *Lgals9* was more broadly expressed (Figures 6C and S8A). To functionally validate these findings, we analyzed spleens from Gdf15$^{-/-}$ mice and littermate controls. Loss of *Gdf15* reduced MMM numbers and increased CD163^{high} RPMs, while MZMs and WPMs remained unchanged (Figures 6D–6G, S8B, and S8C). In contrast, macrophage-specific deletion of *Igf1* using *Tnfrsf11a*^{Cre}; *Igf1*$^{flox/flox}$ (Igf1KO) mice[45] did not alter splenic macrophage composition at baseline (Figures S8D–S8H), indicating that *Igf1* is dispensable for macrophage subset maintenance in homeostasis.

These data suggested that malaria induced lasting alterations in RPM^{iron}/CD163^{high} RPM function, characterized by reduced *Gdf15* expression and impaired niche support for MMM survival. This shift was accompanied by transcriptional adaptations within MMMs consistent with increased self-maintenance, highlighting *Gdf15*-dependent signaling as a key axis controlling splenic macrophage homeostasis.

Please cite this article in press as: Mauel et al., CD163+ red pulp macrophages interact with marginal metallophilic macrophages during blood-stage malaria to maintain splenic architecture, Immunity (2026), https://doi.org/10.1016/j.immuni.2026.07.006

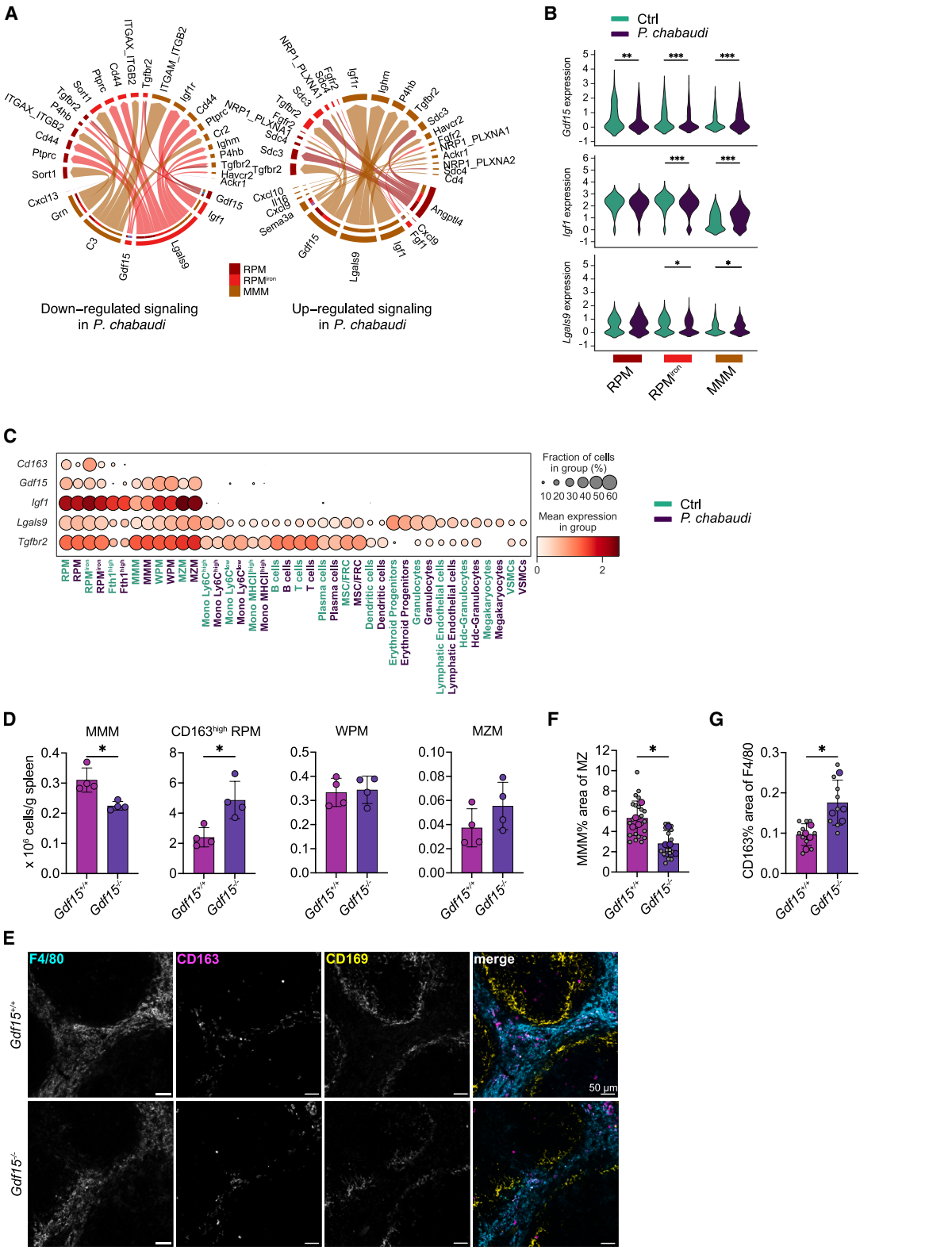

Figure 6. RPM-derived GDF15 sustains MMMs and is suppressed after malaria

(A) Chord diagram showing ligand-receptor interactions between RPM^{iron}, RPMs, and MMMs, showing signaling changes upon *P. chab* infection.

(B) *Lgals9*, *Igf1*, and *Gdf15* expression in RPM^{iron}, RPMs, and MMMs. Mann-Whitney test with two-sided comparison, $^{*}p < 0.05$, $^{**}p < 0.01$, $^{***}p < 0.001$.

(legend continued on next page)

Please cite this article in press as: Mauel et al., CD163+ red pulp macrophages interact with marginal metallophilic macrophages during blood-stage malaria to maintain splenic architecture, Immunity (2026), https://doi.org/10.1016/j.immuni.2026.07.006

MZMs sustain RPM CD163 expression and erythropoietic recovery

To investigate whether MMMs provide reciprocal signals that support RPM maintenance, we genetically depleted MMMs and MZMs by targeting their Lxrα dependence.[4] Conditional KO mice were generated by crossing *Tnfrsf11a*$^{Cre/+}$ with *Lxra*$^{fl/fl}$ mice (hereafter referred to as LxraKO), using Cre-negative littermates as controls (LxraWT). Effective loss of MMMs and MZMs in LxraKO spleens was evident at steady state and during infection (Figure 7A). While MMMs and MZMs remained absent in LxraKO mice at 14 and 35 dpi, LxraWT mice partially recovered both subsets by 35 dpi. Despite the absence of MMMs and MZMs, uninfected LxraKO mice preserved splenic architecture, including separation of red and white pulp regions (Figure 7B) and preserved WPM counts (Figure S8I). Total F4/80$^+$ RPM numbers were similar across genotypes under steady-state conditions, but CD163^{high} RPMs were significantly reduced in LxraKO spleens (Figure 7C), mimicking the post-infection phenotype in WT animals. Similarly, splenic iron stores were reduced in LxraKO mice (Figures S8J and S8K). Immunofluorescence confirmed the reduction of CD163^{high} RPMs and loss of CD169$^+$ MMMs in LxraKO spleens (Figure 7D). Despite broad *Lxra* expression in macrophages in controls and 90 dpi spleens (Figure S8L), CD163^{high} RPM development was unaffected in LxraKO mice over the first 2 postnatal weeks, indicating that this population establishes independently of LXRα and early MMMs loss (Figure S8M).

To assess the functional consequences during infection, we examined spleens between 14 and 35 dpi with *P. chabaudi*. LxraKO mice showed significantly higher parasitemia than LxraWT controls during the second peak (Figure 7E). Whereas LxraWT mice developed splenomegaly at 14 dpi with partial recovery by 35 dpi, LxraKO spleen size remained unchanged and was lower at 14 dpi than in infected LxraWT controls, indicating a blunted splenic response (Figure 7F). Erythropoietic recovery was also defective: both genotypes showed increased circulating WBCs and anemia following *P. chabaudi* infection, as evidenced by reduced RBC counts, hemoglobin concentrations, and hematocrit values at 14 dpi (Figure7G). However, while LxraWT mice exhibited a physiological recovery between 14 and 35 dpi, with increasing RBC counts, hemoglobin concentrations, and a trend toward hematocrit restoration, this response was abrogated in LxraKO mice. Hemoglobin concentrations in LxraKO animals remained significantly reduced at 35 dpi, comparable with values at 14 dpi, and hematocrit values declined further over time (Figure 7G). These findings indicate a failure to restore erythropoiesis in the absence of MZMs and MMMs. In summary, long-term changes to macrophages in the splenic marginal zone result in an inability of RPMs to express CD163 and to ensure proper splenic and erythropoietic recovery following blood-stage malaria.

DISCUSSION

In this study, we provide an in-depth characterization of splenic macrophage subsets and uncover a heterogeneity within RPMs, defined by CD163 expression. To dissect the ontogeny and turnover dynamics of splenic macrophages, we employed both the widely used *Cxcr4*^{CreERT2} model[14,46,47] and our recently established double fate-mapping system.[48] While *Cxcr4*^{CreERT2}-based tracing suggested increasing recruitment of BM-derived cells to both CD163^{high} and CD163$^-$ RPMs during adulthood, the double fate-mapping approach provided a more nuanced picture. Our data demonstrate that both subsets maintain a substantial yolk sac-derived component during early adulthood. In aged animals, long-lived monocyte-derived cells increasingly contributed to both populations. However, CD163^{high} RPMs consistently retained a stronger yolk sac-derived contribution, indicating distinct developmental trajectories between RPM subsets.

The double fate-mapper further revealed substantial ontogenetic heterogeneity among MMMs, MZMs, and WPMs. Consistent with previous studies,[6,49] WPMs were largely monocyte-derived, although we additionally identified a small yolk sac-derived fraction. MZMs showed constant replenishment by monocytes. The ontogenetic profile of MZMs remained stable upon infection, with both short-lived and longer-lived monocyte-derived cells. Yolk sac-derived cells were nearly absent both at steady state and after infection, consistent with a niche that is continuously open and maintained by monocyte input. In contrast, MMMs were predominantly yolk sac-derived under homeostatic conditions. Despite their capacity to cross-present blood-borne antigens via MHC class I,[50] this population remained largely inaccessible to newly recruited monocytes. After infection, yolk sac-derived MMMs were replaced by long-lived monocyte-derived macrophages, suggesting that incoming monocytes adopt a long-lived phenotype rather than contributing to an acute response.

CD163^{high} RPMs emerge as a transcriptionally specialized and spatially distinct population localized near the splenic vasculature, consistent with their role in extracellular hemoglobin clearance, erythrophagocytosis, and iron recycling.[6] Their localization suggests that sustained exposure to blood-borne substrates supports CD163 expression and function, similar to observations in other tissues.[51,52] Our observation that *P. chabaudi* infection induced a pronounced expansion of RPMs differs from previous reports describing RPM depletion

(C) Expression of *Cd163*, *Gdf15*, *Nr1h3*, *Igf1*, *Lgals9*, and *Tgfbr2* across all cell types.
(D) Quantification of MMM, CD163^{high} RPM, WPMs, and MZMs in Gdf15$^{+/+}$ (n = 4) and Gdf15$^{-/-}$ (n = 4) mice by flow cytometry. 1 experiment, Mann-Whitney test, *p < 0.05.
(E) Representative immunofluorescence images of Gdf15$^{+/+}$ and Gdf15$^{-/-}$ mice. Scale bar, 50 μm.
(F) Quantification of MMM area within the splenic marginal zone (MZ) comparing Gdf15$^{+/+}$ (n = 24) and Gdf15$^{-/-}$ (n = 18) mice.
(G) Quantification of CD163^{high} RPMs among all macrophages in the red pulp (RP) of Gdf15$^{+/+}$ (n = 10 RP zones) and Gdf15$^{-/-}$ (n = 8 RP zones) mice. For (F)–(G), n = 4 mice per condition, 1 experiment, unpaired Student's t test with Welch's correction, *p < 0.05. In (D), (F), and (G), bar plots represent mean ± SD; individual mice are represented as circles; each MZ/RP area is represented as gray circle.
See also Figure S8.

Please cite this article in press as: Mauel et al., CD163+ red pulp macrophages interact with marginal metallophilic macrophages during blood-stage malaria to maintain splenic architecture, Immunity (2026), https://doi.org/10.1016/j.immuni.2026.07.006

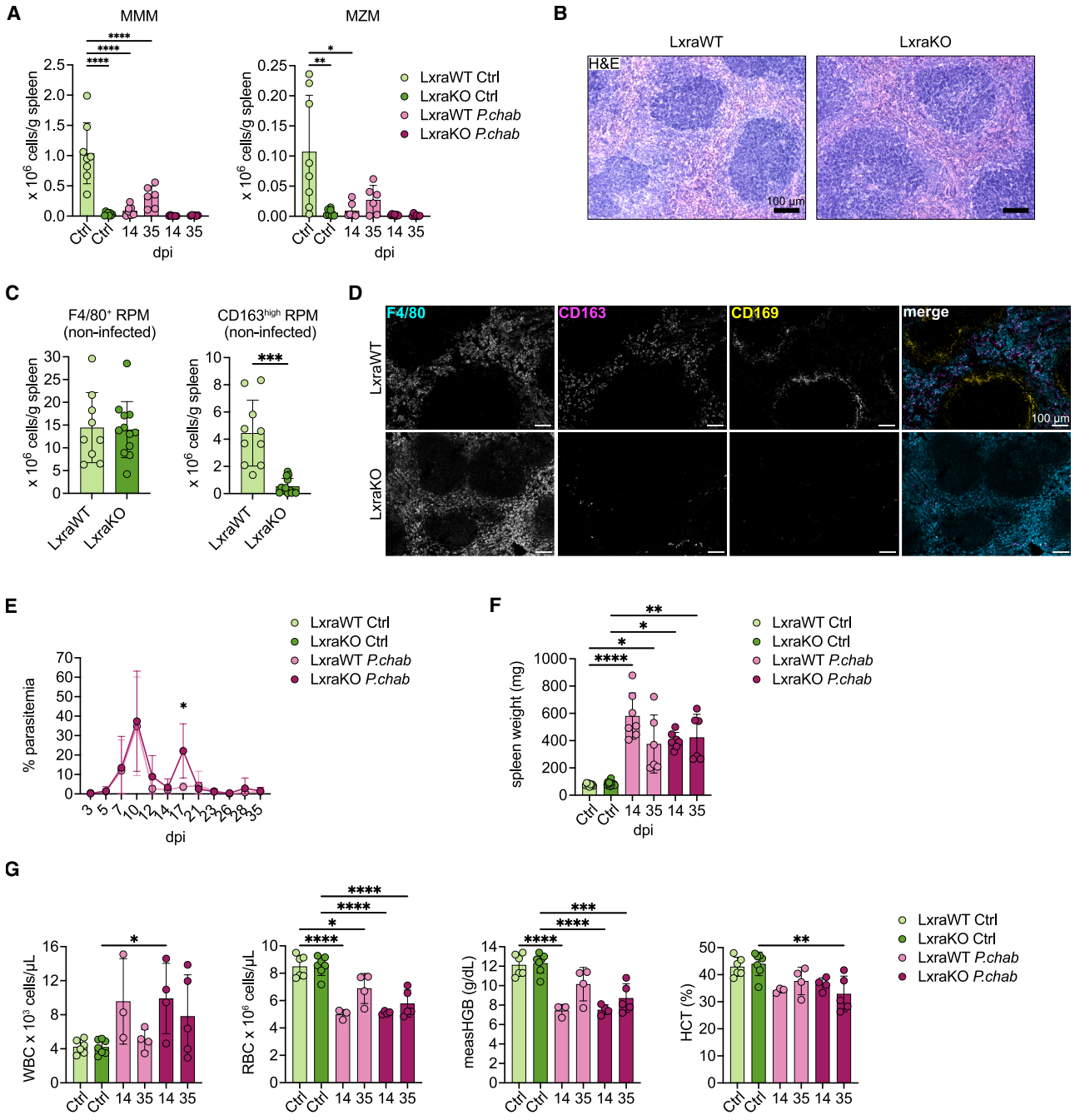

Figure 7. Lxrα deletion depletes marginal zone macrophages, reduces RPM CD163 expression, and impairs erythropoietic recovery after malaria

(A) Quantification of MMMs and MZMs from Tnfrsf11a$^{+/+}$; *Lxra*$^{fl/f}$ (LxraWT) and *Tnfrsf11a*$^{Cre/+}$; *Lxra*$^{fl/f}$ (LxraKO) mice, comparing Ctrl (n [LxraWT] = 9, n [LxraKO] = 10) and *P. chab* infection (n [LxraWT] = 5–6 per time point, n [LxraKO] = 6–7 per time point) at 14 and 35 dpi by flow cytometry. 2–3 independent experiments, one-way ANOVA with multiple comparisons (MMM); Kruskal-Wallis test (MZMs), $^{*}p < 0.05$, $^{**}p < 0.01$, and $^{****}p < 0.0001$.

(B) Representative H&E staining of Ctrl LxraWT and LxraKO. Scale bar, 100 µm. Representative for $n = 4$, 2–3 independent experiments.

(C) Quantification of total RPMs (F4/80^{+}) and CD163^{high} RPMs in non-infected LxraWT and LxraKO mice. n = 9–13, 6 independent experiments, unpaired Student's t test with Welch's correction, $^{***}p < 0.001$.

(D) Representative immunofluorescence images of non-infected LxraWT and LxraKO mice. Scale bar, 100 µm. Representative for $n = 3$, 2–3 independent experiments.

(E) Parasitemia in LxraWT and LxraKO mice. n = 4–15, 2–4 independent experiments, Mann-Whitney test, $^{*}p < 0.05$. Circles represent mean ± SD.

(F) Spleen weights of LxraWT and LxraKO in Ctrl (LxraWT: $n = 9$, LxraKO: $n = 13$) and *P. chab* infection at 14 and 35 dpi (LxraWT: n = 6–7 per time point, LxraKO: n = 6–7 per time point). 3 independent experiments, Kruskal-Wallis test, $^{*}p < 0.05$, $^{**}p < 0.01$, and $^{****}p < 0.0001$.

(legend continued on next page)

Please cite this article in press as: Mauel et al., CD163+ red pulp macrophages interact with marginal metallophilic macrophages during blood-stage malaria to maintain splenic architecture, Immunity (2026), https://doi.org/10.1016/j.immuni.2026.07.006

during infection.[5,53] One explanation may be the differences in parasite inoculum and virulence,[54] with 1×10^4 parasites used in our study compared with 2×10^6 in previous work.[5]

The mechanisms underlying persistent loss of CD163 expression remain incompletely understood. CD163, a receptor expressed by macrophages in both humans and mice, is released from the cell surface in response to inflammatory stimuli, pathogen recognition,[55] TLR ligands,[56,57] and cytokines.[58] We observed a transient increase in circulating CD163 early after *P. chabaudi* and *P. yoelii* infection, followed by an absence at later time points. Receptor release may thus drive the early loss of surface CD163, potentially buffering systemic inflammation,[55] consistent with the partial, reversible reduction of CD163 on RPMs seen in viral (LCMV) and bacterial (LPS) models, where the receptor is lost rather than the population. Malaria-induced loss, however, was more profound and persistent, pointing to additional regulation. Phenylhydrazine-induced hemolysis phenocopies the loss of CD163^{high} RPMs and splenic iron stores, linking this population to the iron-heme axis. Despite normalization of spleen architecture and iron content after recovery, CD163^{high} RPMs failed to fully recover, raising the possibility that their maintenance requires a niche-specific signal that was no longer available. Several mechanisms could account for this failure: (1) long-term remodeling of the splenic niche that impairs local cues needed for CD163 translation in CD163^{iron} cells; (2) transcriptional or post-transcriptional repression within monocyte-derived cells entering the niche; and (3) BM imprinting through the infection that alters the differentiation trajectory of incoming monocytes.

Despite lower splenic iron stores at steady state in *Cd163*$^{-/-}$ mice, they controlled the initial parasitemia peak similarly to controls, indicating that CD163 is dispensable for erythrophagocytic clearance mechanisms. *Cd163*$^{-/-}$ animals experience the first and highest peak of parasitemia without the release of CD163, and clarifying whether this missing checkpoint drives long-term vulnerability to repeated hemolytic stress will be an important goal for future work. During acute infection, however, MMMs were selectively lost, suggesting an infection-dependent dialogue between CD163^{high} RPMs and MMMs that supports optimal splenic responses. Functional validation identified Gdf15 as a non-redundant regulator of MMM homeostasis, as *Gdf15*-deficient mice displayed a selective reduction of MMMs accompanied by a reciprocal increase in CD163^{high} RPMs already under steady-state conditions. These findings establish Gdf15 as a regulator of the RPM-MMM niche and suggest that malaria-induced suppression of *Gdf15* in RPM^{iron}/CD163^{high} RPMs perturbs this trophic support axis.

The inter-dependence of macrophage populations became even more evident in LxraKO mice, indicating that MMMs and/or MZMs are necessary to maintain CD163 expression on RPMs. The combined absence of MMM/MZM niches and CD163 expression on RPMs translated into poorer outcomes after malaria challenge. These findings suggest that recovery from hemolytic stress depends on coordinated interactions between macrophages rather than isolated functions of individual populations.

Our data highlight that malaria triggers not only a temporary loss of immune homeostasis but a fundamental and sustained rewiring of the tissue-resident macrophage network. Even after parasite clearance, the absence of CD163^{high} RPMs and altered communication with MMMs leave a lasting imprint on the splenic microenvironment. These changes may affect secondary immune responses, antigen filtering, iron recycling, and vaccine responsiveness, especially in endemic regions. By showing that macrophage subsets engage in reciprocal trophic support sensitive to specific infectious stressors, this work opens new avenues for targeting tissue immunity and resilience in chronic or relapsing infections.

Limitations of the study

A limitation in translating these findings to humans is the restricted access to tissue-resident macrophages. Most human studies rely on circulating biomarkers measured in blood; thus, CD163 biology has been primarily characterized in circulating monocytes and soluble CD163 concentrations, which correlate with hemolysis, inflammation, and malaria severity.[59–61] However, CD163 release differs between species, with human CD163 predominantly shed as a soluble ectodomain, and murine CD163 released via extracellular vesicles. CD163 is highly expressed by human RPMs and commonly used as a marker for this population,[62,63] suggesting that CD163-dependent macrophage circuits may also exist in human spleen. Whether analogous macrophage circuits operate in human malaria, and how they can be inferred from blood-based measurements, therefore represents an important direction for future studies.

RESOURCE AVAILABILITY

Lead contact

Requests for further information and resources should be directed to and will be fulfilled by the lead contact, Elvira Mass (elvira.mass@uni-bonn.de).

Materials availability

This study did not generate new, unique reagents, and there are no restrictions on data availability. Any other information on materials will be provided upon request to the lead contact.

Data and code availability

The raw transcriptome files and the count data have been deposited in NCBI's Gene Expression Omnibus (GEO). Accession numbers are listed in the key resources table. The data are publicly available from the date of publication. This study did not generate new code. Any additional information required to reanalyze the data reported in this paper is available from the lead contact upon request.

ACKNOWLEDGMENTS

We thank Cornelia Cygon, Akram Abdulkadyrov, Linda Müller, Nikola Makdissi, and Marina Mayer for their support in the lab; Yasuhiro Kobayashi for

(G) Blood parameters (red blood cell [RBC]-count, hemoglobin [HGB], hematocrit [HCT], white blood cell count [WBC]), in LxraWT and LxraKO in Ctrl (LxraWT: n =9, LxraKO: n = 13) and *P. chab* infection at 14 and 35 dpi (LxraWT: n = 6–7 per time point, LxraKO: n = 6–7 per time point). 2 independent experiments, one-way ANOVA with multiple comparisons, $^*p < 0.05$, $^{**}p < 0.01$, $^{***}p < 0.001$, and $^{****}p < 0.0001$. In (A), (C), (F), and (G), bars represent mean ± SD; individual mice are represented as circles.
See also Figure S8.

providing *Tnfrsf11a*^{Cre} mice; Lisa Steinheuer for the alignment of the scRNA-seq data; Kevin Couper for providing the initial parasites stocks; Anders Etzerodt for providing the CD163-ATTO antibody; and Takahiro Asatsuma, Yannick Alexandre, and Thomas Burn for providing LCMV infected spleen samples. The work in the labs was supported by the following grants: the Deutsche Forschungsgemeinschaft (DFG, German Research Foundation) under Germany's Excellence Strategy-EXC2151 (390873048 to E.M.), SFB1454 (project number 432325352 to E.M.), IRTG program GRK2168 (project-ID 272482170 to E.M.), FOR5547 (project ID 503306912 to E.M.), FOR5775 (project ID 533863915 to E.M.); European Research Council (ERC) under the European Union's Horizon 2020 research and innovation program (grant agreement no. 851257 to E.M.); NH&MRC (grant-ID 2002682 to L.B.); ARC (DP240102812 to L.B.); and PhD-fellowship from Boehringer Ingelheim Fonds (to K.M.). We thank the GeneCore at EMBL for technical support and infrastructure, the Gene Editing Core Facility at the University of Bonn for generation of the *CD163*$^{-/-}$ line, the histology core facility at the Medical Sciences Faculty at the University of Bonn, and the Flow Cytometry Core Facility of the Mathematical and Natural Sciences Faculty at the University of Bonn for providing support and instrumentation funded by the DFG (project numbers 553871908, 553871989, 341039622, and 144734146).

AUTHOR CONTRIBUTIONS

K.M. performed experiments, analyzed data, created figures, and wrote the manuscript; D.H., M.-L.D.-W., T.E., and S.L. performed experiments and analyzed data; N.B.-S. performed experiments, analyzed data, and created figures for scRNA-seq; S.N.B. and V.W.-W.T. provided Gdf15$^{-/-}$ spleen samples. M.P.S. supported iron metabolism assays; F.G. provided *Ms4a3*^{FlpO} mice; W.H. provided funding and supervision; and E.M. and L.B. conceptualized the study, analyzed data, created figures, wrote the manuscript, and provided funding. All authors contributed to and reviewed the manuscript.

DECLARATION OF INTERESTS

S.N.B. is an inventor on patents, licensed by St. Vincent's Hospital, on the diagnostic and therapeutic applications of GDF15.

DECLARATION OF GENERATIVE AI AND AI-ASSISTED TECHNOLOGIES IN THE WRITING PROCESS

During the preparation of this work, the authors used ChatGPT in order to edit and improve the readability of some text. After using this tool, the authors reviewed and edited the content as needed and take full responsibility for the content of the published article.

STAR★METHODS

Detailed methods are provided in the online version of this paper and include the following:

SUPPLEMENTAL INFORMATION

Supplemental information can be found online at https://doi.org/10.1016/j.immuni.2026.07.006.

Received: July 20, 2025
Revised: February 18, 2026
Accepted: July 9, 2026

REFERENCES

1. Lewis, S.M., Williams, A., and Eisenbarth, S.C. (2019). Structure and function of the immune system in the spleen. Sci. Immunol. *4*, eaau6085. https://doi.org/10.1126/SCIIMMUNOL.AAU6085.
2. Borges Da Silva, H., Fonseca, R., Pereira, R.M., Cassado, A.A., Álvarez, J.M., and D'Império Lima, M.R. (2015). Splenic macrophage subsets and their function during blood-borne infections. Front. Immunol. *6*, 158939. https://doi.org/10.3389/FIMMU.2015.00480/TEXT.
3. Rahman, Z.S.M., Shao, W.-H., Khan, T.N., Zhen, Y., and Cohen, P.L. (2010). Impaired apoptotic cell clearance in the germinal center by Mer-deficient tingible body macrophages leads to enhanced antibody-forming cell and germinal center responses. J. Immunol. *185*, 5859–5868. https://doi.org/10.4049/JIMMUNOL.1001187.
4. A-Gonzalez, N., Guillen, J.A., Gallardo, G., Diaz, M., de la Rosa, J.V., Hernandez, I.H., Casanova-Acebes, M., Lopez, F., Tabraue, C., Beceiro, S., et al. (2013). The nuclear receptor LXRα controls the functional specialization of splenic macrophages. Nat. Immunol. *14*, 831–839. https://doi.org/10.1038/ni.2622.
5. Wu, Q., Sacomboio, E., Valente de Souza, L., Martins, R., Kitoko, J., Cardoso, S., Ademolue, T.W., Paixão, T., Lehtimäki, J., Figueiredo, A., et al. (2023). Renal control of life-threatening malarial anemia. Cell Rep. *42*, 112057. https://doi.org/10.1016/j.celrep.2023.112057.
6. A-Gonzalez, N., and Castrillo, A. (2018). Origin and specialization of splenic macrophages. Cell. Immunol. *330*, 151–158. https://doi.org/10.1016/J.CELLIMM.2018.05.005.
7. Haldar, M., Kohyama, M., So, A.Y.L., Kc, W., Wu, X., Briseño, C.G., Satpathy, A.T., Kretzer, N.M., Arase, H., Rajasekaran, N.S., et al. (2014). Heme-mediated SPI-C induction promotes monocyte differentiation into iron-recycling macrophages. Cell *156*, 1223–1234. https://doi.org/10.1016/J.CELL.2014.01.069.
8. Kohyama, M., Ise, W., Edelson, B.T., Wilker, P.R., Hildner, K., Mejia, C., Frazier, W.A., Murphy, T.L., and Murphy, K.M. (2009). Role for Spi-C in the development of red pulp macrophages and splenic iron homeostasis. Nature *457*, 318–321. https://doi.org/10.1038/NATURE07472.
9. Poss, K.D., and Tonegawa, S. (1997). Heme oxygenase 1 is required for mammalian iron reutilization. Proc. Natl. Acad. Sci. USA *94*, 10919–10924. https://doi.org/10.1073/PNAS.94.20.10919.
10. Zhang, Z., Zhang, F., An, P., Guo, X., Shen, Y., Tao, Y., Wu, Q., Zhang, Y., Yu, Y., Ning, B., et al. (2011). Ferroportin1 deficiency in mouse macrophages impairs iron homeostasis and inflammatory responses. Blood *118*, 1912–1922. https://doi.org/10.1182/BLOOD-2011-01-330324.
11. Weiss, G., and Goodnough, L.T. (2005). Anemia of Chronic Disease. N. Engl. J. Med. *352*, 1011–1023. https://doi.org/10.1056/NEJMRA041809.
12. Mass, E., Nimmerjahn, F., Kierdorf, K., and Schlitzer, A. (2023). Tissue-specific macrophages: how they develop and choreograph tissue biology.

Nat. Rev. Immunol. *23*, 563–579. https://doi.org/10.1038/S41577-023-00848-Y.

13. Jenkins, S.J., and Allen, J.E. (2021). The expanding world of tissue-resident macrophages. Eur. J. Immunol. *51*, 1882–1896. https://doi.org/10.1002/EJI.202048881.
14. Werner, Y., Mass, E., Ashok Kumar, P., Ulas, T., Händler, K., Horne, A., Klee, K., Lupp, A., Schütz, D., Saaber, F., et al. (2020). Cxcr4 distinguishes HSC-derived monocytes from microglia and reveals monocyte immune responses to experimental stroke. Nat. Neurosci. *23*, 351–362. https://doi.org/10.1038/s41593-020-0585-y.
15. Gentek, R., Ghigo, C., Hoeffel, G., Bulle, M.J., Msallam, R., Gautier, G., Launay, P., Chen, J., Ginhoux, F., and Bajénoff, M. (2018). Hemogenic Endothelial Fate Mapping Reveals Dual Developmental Origin of Mast Cells. Immunity *48*, 1160–1171.e5. https://doi.org/10.1016/j.immuni.2018.04.025.
16. Schulz, C., Perdiguero, E.G., Chorro, L., Szabo-Rogers, H., Cagnard, N., Kierdorf, K., Prinz, M., Wu, B., Jacobsen, S.E.W., Pollard, J.W., et al. (2012). A lineage of myeloid cells independent of myb and hematopoietic stem cells. Science *336*, 86–90. https://doi.org/10.1126/science.1219179.
17. Ginhoux, F., Greter, M., Leboeuf, M., Nandi, S., See, P., Gokhan, S., Mehler, M.F., Conway, S.J., Ng, L.G., Stanley, E.R., et al. (2010). Fate mapping analysis reveals that adult microglia derive from primitive macrophages. Science *330*, 841–845. https://doi.org/10.1126/science.1194637.
18. Yona, S., Kim, K.W., Wolf, Y., Mildner, A., Varol, D., Breker, M., Strauss-Ayali, D., Viukov, S., Guilliams, M., Misharin, A., et al. (2013). Fate mapping reveals origins and dynamics of monocytes and tissue macrophages under homeostasis. Immunity *38*, 79–91. https://doi.org/10.1016/j.immuni.2012.12.001.
19. Gomez Perdiguero, E., Klapproth, K., Schulz, C., Busch, K., Azzoni, E., Crozet, L., Garner, H., Trouillet, C., De Bruijn, M.F., Geissmann, F., et al. (2015). Tissue-resident macrophages originate from yolk-sac-derived erythro-myeloid progenitors. Nature *518*, 547–551. https://doi.org/10.1038/nature13989.
20. Mass, E., Ballesteros, I., Farlik, M., Halbritter, F., Günther, P., Crozet, L., Jacome-Galarza, C.E., Händler, K., Klughammer, J., Kobayashi, Y., et al. (2016). Specification of tissue-resident macrophages during organogenesis. Science *353*, aaf4238. https://doi.org/10.1126/science.aaf4238.
21. Mass, E., and Gentek, R. (2021). Fetal-Derived Immune Cells at the Roots of Lifelong Pathophysiology. Front. Cell Dev. Biol. *9*, 648313. https://doi.org/10.3389/FCELL.2021.648313.
22. Epelman, S., Lavine, K.J., and Randolph, G.J. (2014). Origin and Functions of Tissue Macrophages. Immunity *41*, 21–35. https://doi.org/10.1016/j.immuni.2014.06.013.
23. Sreejit, G., Fleetwood, A.J., Murphy, A.J., and Nagareddy, P.R. (2020). Origins and diversity of macrophages in health and disease. Clin. Transl. Immunology *9*, e1222. https://doi.org/10.1002/CTI2.1222.
24. Rodríguez-Morales, P., and Franklin, R.A. (2023). Macrophage phenotypes and functions: resolving inflammation and restoring homeostasis. Trends Immunol. *44*, 986–998. https://doi.org/10.1016/J.IT.2023.10.004.
25. Fernandez-Ruiz, D., Ng, W.Y., Holz, L.E., Ma, J.Z., Zaid, A., Wong, Y.C., Lau, L.S., Mollard, V., Cozijnsen, A., Collins, N., et al. (2016). Liver-Resident Memory CD8+ T Cells Form a Front-Line Defense against Malaria Liver-Stage Infection. Immunity *45*, 889–902. https://doi.org/10.1016/J.IMMUNI.2016.08.011.
26. Coban, C., Lee, M.S.J., and Ishii, K.J. (2018). Tissue-specific immunopathology during malaria infection. Nat. Rev. Immunol. *18*, 266–278. https://doi.org/10.1038/nri.2017.138.
27. Ghilas, S., Enders, M.H., May, R., Holz, L.E., Fernandez-Ruiz, D., Cozijnsen, A., Mollard, V., Cockburn, I.A., McFadden, G.I., Heath, W.R., et al. (2021). Development of Plasmodium-specific liver-resident memory CD8+ T cells after heat-killed sporozoite immunization in mice. Eur. J. Immunol. *51*, 1153–1165. https://doi.org/10.1002/EJI.202048757.
28. Sponaas, A.M., Freitas do Rosario, A.P.F., Voisine, C., Mastelic, B., Thompson, J., Koernig, S., Jarra, W., Renia, L., Mauduit, M., Potocnik, A.J., et al. (2009). Migrating monocytes recruited to the spleen play an important role in control of blood stage malaria. Blood *114*, 5522–5531. https://doi.org/10.1182/BLOOD-2009-04-217489.
29. Pack, A.D., Schwartzhoff, P.V., Zacharias, Z.R., Fernandez-Ruiz, D., Heath, W.R., Gurung, P., Legge, K.L., Janse, C.J., and Butler, N.S. (2021). Hemozoin-mediated inflammasome activation limits long-lived anti-malarial immunity. Cell Rep. *36*, 109586. https://doi.org/10.1016/J.CELREP.2021.109586.
30. Pamplona, A., Ferreira, A., Balla, J., Jeney, V., Balla, G., Epiphanio, S., Chora, A., Rodrigues, C.D., Gregoire, I.P., Cunha-Rodrigues, M., et al. (2007). Heme oxygenase-1 and carbon monoxide suppress the pathogenesis of experimental cerebral malaria. Nat. Med. *13*, 703–710. https://doi.org/10.1038/nm1586.
31. De Simone, G., Varricchio, R., Ruberto, T.F., di Masi, A., and Ascenzi, P. (2023). Heme Scavenging and Delivery: The Role of Human Serum Albumin. Biomolecules *13*, 575. https://doi.org/10.3390/BIOM13030575.
32. Ramos, S., Jeney, V., Figueiredo, A., Paixão, T., Sambo, M.R., Quinhentos, V., Martins, R., Gouveia, Z., Carlos, A.R., Ferreira, A., et al. (2024). Targeting circulating labile heme as a defense strategy against malaria. Life Sci. Alliance *7*, e202302276. https://doi.org/10.26508/LSA.202302276.
33. Lai, S.M., Sheng, J., Gupta, P., Renia, L., Duan, K., Zolezzi, F., Karjalainen, K., Newell, E.W., and Ruedl, C. (2018). Organ-Specific Fate, Recruitment, and Refilling Dynamics of Tissue-Resident Macrophages during Blood-Stage Malaria. Cell Rep. *25*, 3099–3109.e3. https://doi.org/10.1016/j.celrep.2018.11.059.
34. Schultze, J.L., Mass, E., and Schlitzer, A. (2019). Emerging Principles in Myelopoiesis at Homeostasis and during Infection and Inflammation. Immunity *50*, 288–301. https://doi.org/10.1016/j.immuni.2019.01.019.
35. Etzerodt, A., Mikkelsen, J.H., Torvund-Jensen, M., Hennig, D., Boesen, T., Graversen, J.H., Moestrup, S.K., Kollman, J.M., and Andersen, C.B.F. (2024). The Cryo-EM structure of human CD163 bound to haptoglobin-hemoglobin reveals molecular mechanisms of hemoglobin scavenging. Nat. Commun. *15*, 10871. https://doi.org/10.1038/S41467-024-55171-4.
36. Li, X., Wang, S., Cao, H., Xu, S., Xiong, C., Yu, J., Chen, Y., Ren, Z., Li, M., Hu, Y., et al. (2025). The CD163 + tissue-infiltrating macrophages regulate ferroptosis in thyroid-associated ophthalmopathy orbital fibroblasts via the TGF-β/Smad2/3 signaling pathway. J. Transl. Med. *23*, 423. https://doi.org/10.1186/S12967-025-06443-0.
37. Liu, T., Xu, P., Ke, S., Dong, H., Zhan, M., Hu, Q., and Li, J. (2022). Histone methyltransferase SETDB1 inhibits TGF-β-induced epithelial–mesenchymal transition in pulmonary fibrosis by regulating SNAI1 expression and the ferroptosis signaling pathway. Arch. Biochem. Biophys. *715*, 109087. https://doi.org/10.1016/J.ABB.2021.109087.
38. Bellomo, A., Gentek, R., Golub, R., and Bajénoff, M. (2021). Macrophage-fibroblast circuits in the spleen. Immunol. Rev. *302*, 104–125. https://doi.org/10.1111/IMR.12979.
39. Shen, Y., Li, X., Zhao, B., Xue, Y., Wang, S., Chen, X., Yang, J., Lv, H., and Shang, P. (2018). Iron metabolism gene expression and prognostic features of hepatocellular carcinoma. J. Cell. Biochem. *119*, 9178–9204. https://doi.org/10.1002/jcb.27184.
40. Mauel, K., and Mass, E. (2024). Fate-Mapping of Hematopoietic Stem Cell-Derived Macrophages. Methods Mol. Biol. *2713*, 139–148. https://doi.org/10.1007/978-1-0716-3437-0_9.
41. Hashimoto, D., Chow, A., Noizat, C., Teo, P., Beasley, M.B., Leboeuf, M., Becker, C.D., See, P., Price, J., Lucas, D., et al. (2013). Tissue-resident macrophages self-maintain locally throughout adult life with minimal contribution from circulating monocytes. Immunity *38*, 792–804. https://doi.org/10.1016/j.immuni.2013.04.004.
42. Liu, Z., Gu, Y., Chakarov, S., Bleriot, C., Kwok, I., Chen, X., Shin, A., Huang, W., Dress, R.J., Dutertre, C.-A., et al. (2019). Fate Mapping via Ms4a3-Expression History Traces Monocyte-Derived Cells. Cell *178*, 1509–1525.e19. https://doi.org/10.1016/j.cell.2019.08.009.

43. Ismahil, M.A., Zhou, G., Rajasekar, S., Gao, M., Bansal, S.S., Patel, B., Limdi, N., Xie, M., Antipenko, S., Rokosh, G., et al. (2025). Splenic CD169+Tim4+Marginal Metallophilic Macrophages Are Essential for Wound Healing After Myocardial Infarction. Circulation *151*, 1712–1729. https://doi.org/10.1161/CIRCULATIONAHA.124.071772.

44. Soares, M.P., and Hamza, I. (2016). Macrophages and iron metabolism. Immunity *44*, 492–504. https://doi.org/10.1016/J.IMMUNI.2016.02.016.

45. Makdissi, N., Hirschmann, D.J., Frolov, A., Sado, I., Bennühr, B., Nikolka, F., Cheng, J., Blank-Stein, N., Viola, M.F., Yaghmour, M., et al. (2026). Kupffer cells control neonatal hepatic metabolism via Igf1 signaling. Development *153*, dev204962. https://doi.org/10.1242/DEV.204962.

46. Frolov, A., Huang, H., Schütz, D., Köhne, M., Blank-Stein, N., Osei-Sarpong, C., Büttner, M., Elmzzahi, T., Khundadze, M., Zahid, M., et al. (2025). Microglia and CD8+ T cell activation precede neuronal loss in a murine model of spastic paraplegia 15. J. Exp. Med. *222*, e20232357. https://doi.org/10.1084/jem.20232357.

47. Siret, C., van Lessen, M., Bavais, J., Jeong, H.W., Reddy Samawar, S.K., Kapupara, K., Wang, S., Simic, M., de Fabritus, L., Tchoghandjian, A., et al. (2022). Deciphering the heterogeneity of the Lyve1+ perivascular macrophages in the mouse brain. Nat. Commun. *13*, 7366. https://doi.org/10.1038/S41467-022-35166-9.

48. Huang, H., Balzer, N.R., Seep, L., Splichalova, I., Blank-Stein, N., Viola, M.F., Franco Taveras, E., Acil, K., Fink, D., Petrovic, F., et al. (2025). Kupffer cell programming by maternal obesity triggers fatty liver disease. Nature *644*, 790–798. https://doi.org/10.1038/S41586-025-09190-W.

49. den Haan, J.M.M., and Kraal, G. (2012). Innate Immune Functions of Macrophage Subpopulations in the Spleen. J. Innate Immun. *4*, 437–445. https://doi.org/10.1159/000335216.

50. Mauvais, F.X., Hamel, Y., Silvin, A., Mulder, K., Hildner, K., Akyol, R., Dalod, M., Koumantou, D., Saveanu, L., Garfa, M., et al. (2025). Metallophilic marginal zone macrophages cross-prime CD8+ T cell-mediated protective immunity against blood-borne tumors. Immunity *58*, 843–860.e20. https://doi.org/10.1016/J.IMMUNI.2025.02.027.

51. Jayaraman, V., Prise, I.E., Kästele, V., Tamburrano, S., Wemyss, K., Bridgeman, H.M., Daw, R.H., Strangward, P., Sanderson, A., Cruickshank, S.M., et al. (2026). CD163 and Tim-4 identify resident intestinal macrophages that are spatially regulated by TGF-β. Journal of Experimental Medicine. https://doi.org/10.1084/jem.20240801.

52. Zhan, X., Wang, S., Bèchet, N., Gouras, G., and Wen, G. (2025). Perivascular macrophages in the central nervous system: insights into their roles in health and disease. Cell Death Dis. *16*, 350. https://doi.org/10.1038/s41419-025-07592-2.

53. Nahrendorf, W., Ivens, A., and Spence, P.J. (2021). Inducible mechanisms of disease tolerance provide an alternative strategy of acquired immunity to malaria. eLife *10*, e63838. https://doi.org/10.7554/ELIFE.63838.

54. Spence, P.J., Jarra, W., Lévy, P., Reid, A.J., Chappell, L., Brugat, T., Sanders, M., Berriman, M., and Langhorne, J. (2013). Vector transmission regulates immune control of Plasmodium virulence. Nature *498*, 228–231. https://doi.org/10.1038/NATURE12231.

55. Kuang, H., Dou, G., Cheng, L., Wang, X., Xu, H., Liu, X., Ding, F., Yang, X., Liu, S., Bao, L., et al. (2023). Humoral regulation of iron metabolism by extracellular vesicles drives antibacterial response. Nat. Metab. *5*, 111–128. https://doi.org/10.1038/S42255-022-00723-5.

56. Weaver, L.K., Hintz-Goldstein, K.A., Pioli, P.A., Wardwell, K., Qureshi, N., Vogel, S.N., and Guyre, P.M. (2006). Pivotal Advance: Activation of cell surface Toll-like receptors causes shedding of the hemoglobin scavenger receptor CD163. J. Leukoc. Biol. *80*, 26–35. https://doi.org/10.1189/JLB.1205756.

57. Etzerodt, A., Berg, R.M.G., Plovsing, R.R., Andersen, M.N., Bebien, M., Habbeddine, M., Lawrence, T., Møller, H.J., and Moestrup, S.K. (2017). Soluble ectodomain CD163 and extracellular vesicle-associated CD163 are two differently regulated forms of â €soluble CD163' in plasma. Sci. Rep. *7*, 40286. https://doi.org/10.1038/SREP40286.

58. Etzerodt, A., Maniecki, M.B., Møller, K., Møller, H.J., and Moestrup, S.K. (2010). Tumor necrosis factor α-converting enzyme (TACE/ADAM17) mediates ectodomain shedding of the scavenger receptor CD163. J. Leukoc. Biol. *88*, 1201–1205. https://doi.org/10.1189/JLB.0410235.

59. Bengtsson, E., Hultman, K., Edsfeldt, A., Persson, A., Nitulescu, M., Nilsson, J., Gonçalves, I., and Björkbacka, H. (2020). CD163+ macrophages are associated with a vulnerable plaque phenotype in human carotid plaques. Sci. Rep. *10*, 14362. https://doi.org/10.1038/S41598-020-71110-X.

60. Buechler, C., Ritter, M., Orsó, E., Langmann, T., Klucken, J., and Schmitz, G. (2000). Regulation of scavenger receptor CD163 expression in human monocytes and macrophages by pro- and antiinflammatory stimuli. J. Leukoc. Biol. *67*, 97–103. https://doi.org/10.1002/jlb.67.1.97.

61. Lautenbach, M.J., Wyss, K., Yman, V., Foroogh, F., Satarvandi, D., Mousavian, Z., Sondén, K., Wang, J., Álvez, M.B., Bergström, S., et al. (2025). Systems analysis of clinical malaria reveals proteomic perturbation and innate-adaptive crosstalk linked to disease severity. Immunity *58*, 2120–2136.e5. https://doi.org/10.1016/j.immuni.2025.06.014.

62. Nagelkerke, S.Q., Bruggeman, C.W., den Haan, J.M.M., Mul, E.P.J., Van Den Berg, T.K., Van Bruggen, R., and Kuijpers, T.W. (2018). Red pulp macrophages in the human spleen are a distinct cell population with a unique expression of Fc-γ receptors. Blood Adv. *2*, 941–953. https://doi.org/10.1182/BLOODADVANCES.2017015008.

63. Steiniger, B.S., Pfeffer, H., Guthe, M., and Lobachev, O. (2021). Exploring human splenic red pulp vasculature in virtual reality: details of sheathed capillaries and the open capillary network. Histochem. Cell Biol. *155*, 341–354. https://doi.org/10.1007/S00418-020-01924-3.

64. Tsai, V.W.W., Macia, L., Johnen, H., Kuffner, T., Manadhar, R., Jørgensen, S.B., Lee-Ng, K.K.M., Zhang, H.P., Wu, L., Marquis, C.P., et al. (2013). TGF-b Superfamily Cytokine MIC-1/GDF15 Is a Physiological Appetite and Body Weight Regulator. PLoS One *8*, e55174. https://doi.org/10.1371/journal.pone.0055174.

65. Wolf, F.A., Angerer, P., and Theis, F.J. (2018). SCANPY: Large-scale single-cell gene expression data analysis. Genome Biol. *19*, 15. https://doi.org/10.1186/s13059-017-1382-0.

66. Jin, S., Plikus, M.V., and Nie, Q. (2025). CellChat for systematic analysis of cell-cell communication from single-cell transcriptomics. Nat. Protoc. *20*, 180–219. https://doi.org/10.1038/S41596-024-01045-4.

67. Fang, Z., Liu, X., and Peltz, G. (2023). GSEApy: a comprehensive package for performing gene set enrichment analysis in Python. Bioinformatics *39*, btac757. https://doi.org/10.1093/BIOINFORMATICS/BTAC757.

68. Maeda, K., Kobayashi, Y., Udagawa, N., Uehara, S., Ishihara, A., Mizoguchi, T., Kikuchi, Y., Takada, I., Kato, S., Kani, S., et al. (2012). Wnt5a-Ror2 signaling between osteoblast-lineage cells and osteoclast precursors enhances osteoclastogenesis. Nat. Med. *18*, 405–412. https://doi.org/10.1038/nm.2653.

69. Srinivas, S., Watanabe, T., Lin, C.S., William, C.M., Tanabe, Y., Jessell, T.M., and Costantini, F. (2001). Cre reporter strains produced by targeted insertion of EYFP and ECFP into the ROSA26 locus. BMC Dev. Biol. *1*, 4. https://doi.org/10.1186/1471-213X-1-4.

70. Daigle, T.L., Madisen, L., Hage, T.A., Valley, M.T., Knoblich, U., Larsen, R.S., Takeno, M.M., Huang, L., Gu, H., Larsen, R., et al. (2018). A suite of transgenic driver and reporter mouse lines with enhanced brain-cell-type targeting and functionality. Cell *174*, 465–480.e22. https://doi.org/10.1016/J.CELL.2018.06.035.

71. Mueller, S.N., Matloubian, M., Clemens, D.M., Sharpe, A.H., Freeman, G.J., Gangappa, S., Larsen, C.P., and Ahmed, R. (2007). Viral targeting of fibroblastic reticular cells contributes to immunosuppression and persistence during chronic infection. Proc. Natl. Acad. Sci. USA *104*, 15430–15435. https://doi.org/10.1073/PNAS.0702579104.

72. Mbanwi, A.N., Wang, C., Geddes, K., Philpott, D.J., and Watts, T.H. (2017). Irreversible splenic atrophy following chronic LCMV infection is associated with compromised immunity in mice. Eur. J. Immunol. *47*, 94–106. https://doi.org/10.1002/EJI.201646666.

73. Wherry, E.J., Blattman, J.N., Murali-Krishna, K., van der Most, R., and Ahmed, R. (2003). Viral persistence alters CD8 T-cell immunodominance and tissue distribution and results in distinct stages of functional impairment. J. Virol. *77*, 4911–4927. https://doi.org/10.1128/JVI.77.8.4911-4927.2003.

74. Leon, L.R., Kozak, W., Rudolph, K., and Kluger, M.J. (1999). An antipyretic role for interleukin-10 in LPS fever in mice. Am. J. Physiol. *276*, R81–R89. https://doi.org/10.1152/ajpregu.1999.276.1.r81.

75. McInnes, L., Healy, J., Saul, N., and Großberger, L. (2018). UMAP: Uniform Manifold Approximation and Projection. J. Open Source Softw. *3*, 861. https://doi.org/10.21105/JOSS.00861.

76. Schindelin, J., Arganda-Carreras, I., Frise, E., Kaynig, V., Longair, M., Pietzsch, T., Preibisch, S., Rueden, C., Saalfeld, S., Schmid, B., et al. (2012). Fiji: an open-source platform for biological-image analysis. Nat. Methods *9*, 676–682. https://doi.org/10.1038/NMETH.2019.

77. Wolock, S.L., Lopez, R., and Klein, A.M. (2019). Scrublet: Computational Identification of Cell Doublets in Single-Cell Transcriptomic Data. Cell Syst. *8*, 281–291.e9. https://doi.org/10.1016/j.cels.2018.11.005.

78. Tirosh, I., Izar, B., Prakadan, S.M., Wadsworth, M.H., III, Treacy, D., Trombetta, J.J., Rotem, A., Rodman, C., Lian, C., Murphy, G., et al. (2016). Dissecting the multicellular ecosystem of metastatic melanoma by single-cell RNA-seq. Science *352*, 189–196. https://doi.org/10.1126/science.aad0501.

Please cite this article in press as: Mauel et al., CD163+ red pulp macrophages interact with marginal metallophilic macrophages during blood-stage malaria to maintain splenic architecture, Immunity (2026), https://doi.org/10.1016/j.immuni.2026.07.006

STAR★METHODS

KEY RESOURCES TABLE

REAGENT or RESOURCE	SOURCE	IDENTIFIER
Antibodies		
CD115 - APC (clone AFS98)	Biolegend	Cat# 135510; RRID: AB_2085221
CD11b - BUV536 (clone M1/70)	BD Biosciences	Cat# 569711; RRID: AB_3685254
CD11b – BUV661 (clone M1/70)	BD Biosciences	Cat# 612977; RRID: AB_2870249
CD11b – PE-Cy7 (clone M1/70)	Biolegend	Cat# 101216; RRID: AB_312799
CD11c – BV605 (N418)	Biolegend	Cat# 117333; RRID: AB_11204262
CD127 – PerCP/Cy5.5 (clone A7R34)	Biolegend	Cat# 135022; RRID: AB_1937273
CD135 – BV421 (A2F10)	Biolegend	Cat# 135313; RRID: AB_2562338
CD150 (SLAM) – PE-Cy7 (clone TC15-12F12.2)	Biolegend	Cat# 115914; RRID: AB_439797
CD16/32 – APC-Cy7 (clone 93)	Biolegend	Cat# 101328; RRID: AB_2104158
CD163 – BV421 (clone S15049I)	Biolegend	Cat# 155309; RRID: AB_2814063
CD169 – BV605 (clone 3D6.112)	Biolegend	Cat# 142413; RRID: AB_2564030
CD169 – BV605 (clone 3D6.112)	Biolegend	Cat# 142413; RRID AB_2 564030
CD172a – PE-Cy7 (clone P84)	Biolegend	Cat# 144008; RRID: AB_2563546
CD19 – APC-Cy7 (clone 6D5)	Biolegend	Cat# 115530; RRID: AB_830707
CD19 – Biotin (clone 6D5)	Biolegend	Cat# 115504; RRID: AB_313639
CD19 – BV421 (clone 6D5)	Biolegend	Cat# 115537; RRID: AB_10895761
CD209b – BV711 (clone 22D1)	BD Biosciences	Cat# 756161; RRID: AB_3688416
CD34 – AF700 (clone RAM43)	BD Biosciences	Cat# 560518; RRID: AB_1727471
CD45 – APC (clone 30-F11)	Biolegend	Cat# 103112; RRID: AB_312977
CD45 – BUV805 (clone 30-F11)	BD Biosciences	Cat# 568336; RRID: AB_3684191
CD48 – AF647 (clone HM48-1)	Biolegend	Cat# 103416; RRID: AB_571987
CD64 – PerCP/Cy5.5 (clone X54-5/7.1)	Biolegend	Cat# 139308; RRID: AB_2561963
CD64 – PerCP/Cy5.5 (clone X54-5/7.1)	Biolegend	Cat# 139308; RRID: AB_2561963
Draq7 – APC-Cy7	Biolegend	Cat# 424001
F4/80 - APC/Cy7 (clone BM8)	Biolegend	Cat#123118; RRID: AB_893447
F4/80 – BV421 (clone BM8)	Biolegend	Cat# 123132; RRID: AB_11203717
Gr1 – Biotin (clone RB6-8C5)	Biolegend	Cat# 108404; RRID: AB_313369
Kit (CD117) – BV711 (clone 2B8)	Biolegend	Cat# 105835; RRID: AB_2565956
Ly6C – BV510 (clone HK1.4)	Biolegend	Cat# 128033; RRID: AB_2562351
Ly6G – APC-Cy7 (clone 1A8)	Biolegend	Cat# 127624; RRID: AB_10640819
Ly6G – Biotin (clone 1A8)	Biolegend	Cat# 127604; RRID: AB_1186108
Ly6G – PerCP/Cy5.5 (clone 1A8)	Biolegend	Cat# 127616; RRID: AB_1877271
MARCO – APC (clone 579511)	R&D Systems	Cat# FAB2956A
MerTK – PE-Cy7 (clone 2B10C42)	Biolegend	Cat# 151522
MHCII – AF700 (clone M5/114.15.2)	Biolegend	Cat# 107622; RRID: AB_493727
Nkp46 – APC-Cy7 (clone 29A1.4)	Biolegend	Cat# 137646; RRID: AB_11218796
NKp46 – Biotin (clone 29A1.4)	Biolegend	Cat# 137616; RRID: AB_11218796
Nkp46 – BV711 (clone 29A1.4)	Biolegend	Cat# 137621; RRID: AB_2563289
Sca1 – BV510 (clone D7)	Biolegend	Cat# 108129; RRID: AB_2561593
Streptavidin – BV785	Biolegend	Cat# 405249
TCR-beta – APC-Cy7 (clone H57-597)	Biolegend	Cat# 109220; RRID: AB_893624
TCR-beta – Biotin (clone H57-597)	Biolegend	Cat# 109204; RRID: AB_313427
Ter119 – Biotin (clone TER-119)	Biolegend	Cat# 116204; RRID: AB_313705
Tim4 - BUV563 (clone RMT4-54)	BD Biosciences	Cat# 749135; RRID: AB_2873524

(*Continued on next page*)

Please cite this article in press as: Mauel et al., CD163+ red pulp macrophages interact with marginal metallophilic macrophages during blood-stage malaria to maintain splenic architecture, Immunity (2026), https://doi.org/10.1016/j.immuni.2026.07.006

Continued

REAGENT or RESOURCE	SOURCE	IDENTIFIER
XCR1 – APC-Cy7 (clone ZET)	Biolegend	Cat# 148224; RRID: AB_2783118
α-a.Hamster – DyLight 649 (clone Poly4055)	Biolegend	Cat# 405505; RRID: AB_1575122
α-chicken – AF488	Thermo Fisher Scientific	Cat# A78948; RRID: AB_2921070
α-rabbit – AF488	Thermo Fisher Scientific	Cat# A-11008; RRID: AB_143165
α-rat – AF488	Thermo Fisher Scientific	Cat# A-11006; RRID: AB_2534074
α-rat – AF555	Thermo Fisher Scientific	Cat# A78945; RRID: AB_2910652
α-rat – AF647	Biolegend	Cat# A78947
CD163 – ATTO-647	Anders Etzerodt	
CD163 (clone TNKUPJ)	Thermo Fisher Scientific	Cat# 14-1631-82; RRID: AB_2716934
CD163 – PE (clone S15049I)	Biolegend	Cat# 155308; RRID: AB_2814062
CD169 (Signlec-1) – Biotin (clone REA197 | 3D6.112)	Miltenyi Biotec	Cat# 130-121-441; RRID: AB_2889469
CD31 – AF488 (clone MEC13.3)	Biolegend	Cat# 102514; RRID: AB_2161031
CD31 (armenian Hamster) – AF488 (clone 2H8)	Thermo Fisher Scientific	Cat# MA3105; RRID: AB_223592
F4/80 (chicken, clone EPR26545-166)	Abcam	Cat# ab320060
F4/80 (rat, clone CI:A3-1)	BIO-RAD	Cat# MCA497GA; RRID: AB_323806
Iba1 (rabbit, clone EPR16589)	Abcam	Cat# ab178847; RRID: AB_2832244
Streptavidin - PE	Biolegend	Cat# 405203
Streptavidin – AF647	Biolegend	Cat# 405237
GFP (Rat, clone GF090R)	Biotechnik Gerbu	Cat# 04404
Bacterial and virus strains		
LCMV	R. Ahmed, Emory University	NCBITaxon_11624
LPS (from E.coli 0111:B4)	InvivoGen	Cat# tlrl-eblps
Biological samples		
Plasmodium chabaudi AS	Kevin Couper, Manchester	NCBITaxon_31271
Plasmodium yoelii 17XNL	QIMR Brisbane	NCBITaxon_1323249
Plasmodium berghei ANKA	Walter and Eliza Hall Institute	NCBITaxon_5823
Chemicals, peptides, and recombinant proteins		
Phenyl-hydrazine	Sigma-Aldrich	Cat# P26252
Tamoxifen	Sigma-Aldrich	Cat# T5648
Chloroquine	Sigma-Aldrich	Cat# C6628
Hoechst	ThermoFisher Scientific	Cat# H1398
DAPI	Biolegend	Cat# 42281
DNase	Sigma-Aldrich	Cat# DN25
Dispase	Gibco	Cat# 17105041
Collagenase D	Roche	Cat# 11088858001
Entellan	Millipore	Cat# 1.07961.0100
Formaldehyde	ThermoFisher Scientific	Cat# 11586711
D-Sucrose	ThermoFisher Scientific	Cat# 10638403
Tissue-Tek O.C.T.	Sakura Finetek	Cat# 4583
Triton X-100	Sigma-Aldrich	Cat# X100
BSA	ThermoFisher Scientific	Cat# 37525
Donkey-serum	Sigma-Aldrich	Cat# D9663
Flavopiridol	Sigma-Aldrich	Cat# F3055
Ascorbic acid	AppliChem	Cat# A1052,0100
Bathophenanthroline disulfonic acid ($C_{24}H_{16}N_2O_6S_2$)	Sigma-Aldrich	Cat# B1375-500MG
Hydrogen Chloride (HCl)	VWR	Cat# 20252.290
Iron (II) sulfate heptahydrate ($FeH_{14}O_{11}S$)	Sigma-Aldrich	Cat# F-8633
Sodium acetate (NaOAc) (CH_3COONa)	Sigma-Aldrich	Cat# S2889-250G
Trichloroacetic acid (TCA) ($C_2HCl_3O_2$)	Sigma-Aldrich	Cat# 1.00807.0100

(*Continued on next page*)

Please cite this article in press as: Mauel et al., CD163+ red pulp macrophages interact with marginal metallophilic macrophages during blood-stage malaria to maintain splenic architecture, Immunity (2026), https://doi.org/10.1016/j.immuni.2026.07.006

Continued

REAGENT or RESOURCE	SOURCE	IDENTIFIER
Critical commercial assays		
ELISA (sCD163)	Abcam	Cat# ab272204
Mouse CD45 microbeads	Miltenyi Biotec	Cat# 130-052-301
10x Genomics Chromium Controller and the Chromium Next GEM Single cell 3' Reagent Kit v3.1 (Dual Index) (PN-1000268, 10x Genomics, Pleasanton, CA, USA)	10x Genomics	Cat# PN-1000268; Components: PN-1000204, PN-1000121, PN-1000127, PN-1000215
Qubit 4 Fluorometer	Thermo Fisher Scientific	Cat# Q33226
Qubit™ 1X dsDNA HS Assay Kit	Thermo Fisher Scientific	Cat# Q33231
Beckman Coulter SPRIselect 60 mL reagent kit	Beckman Coulter	Cat# B23318
High Sensitivity DNA ScreenTape Analysis	Agilent Technologies	Cat# 5067-5592
Deposited data		
Database GEO	This study	Accession number GSE303987
Experimental models: Organisms/strains		
Mouse: WT C57BL/6JRccHsd	Inotiv	JAX #000664
Mouse (DFM): STOCK-*Tnfrsf11a<tm1 (EGFP/cre)Ykob> Gt(ROSA)26Sor<tm1 (EYFP)Cos> Gt(ROSA)26Sor<tm65.2 (CAG-tdTomato)Hze> Ms4a3<tm3 (IRES-Flp-pA-fnf)Smoc>*/Emass	DFM: this paper, Parental lines: *Tnfrsf11a*^{Cre}: Yasuhiro Kobayashi, *Rosa26*$^{LSL-YFP}$, *Rosa26*$^{FSF-tdTomato}$: The Jackson Laboratory, Ms4a3^{FlpO}: Florent Ginhoux	MGI:5316980, MGI:2449038, MGI:6260212, N/A
Mouse:*Cxcr4*^{CreERT}*; Rosa26*$^{LSL-tdTomato}$: B6J.Cg-*Cxcr4<tm1.1(cre/ERT2)Stum> Gt(ROSA)26Sor<tm14(CAG-tdTomato) Hze>*/Emass	This Paper, Parental lines: *Cxcr4*^{CreERT}: Werner et al.[14] *Rosa26*$^{LSL-tdTomato}$: The Jackson Laboratory	MGI:6719054 MGI:3809524
Mouse: Lxrafl$^{/fl}$*; Tnfrsf11a*^{Cre}: STOCK-*Tnfrsf11a<tm1(EGFP/cre) Ykob> Nr1h3<tm1.1Ics>*/Emass	This Paper, Parental lines: *Lxra*$^{fl/fl}$*:* Institut Clinique de la Souris, *Tnfrsf11a*^{Cre}: Yasuhiro Kobayashi	MGI:5316980, MGI:6467790
Mouse: *Cd163*$^{-/-}$: B6JRcc; B6J-*CD163*^{em1Limes}/Emass	This paper	N/A
Mouse: Igf1fl$^{/fl}$*; Tnfrsf11a*^{Cre}: STOCK-Tnfrsf11a<tm1(EGFP/cre) Ykob> Igf1<tm1Dlr>/Emass	This Paper, Parental lines: *Igf1*$^{fl/fl}$*:* The Jackson Laboratory, *Tnfrsf11a*^{Cre}: Yasuhiro Kobayashi	MGI:5316980, MGI:2152423
Mouse: Gdf15$^{-/-}$	Mice were generated as previously described: Tsai et al.[64]	N/A
Oligonucleotides		
Primers, see Table S6	This paper	N/A
Single-guide RNA for CD163 knockout: sg1: TGGGCTGCACGTAAACAATAAACAGTTG TATTTCTGAAGTTGTTCTACCAGCCCTG TATAACTTCGTATAGCATACATTA TACGAAGTTATGAATTCGTTCTCG ATCGGAATCTTTCCCACTTGCCAA AGGAAGGGTCTTTCTTTGTCTTGG	This paper	N/A
Single-guide RNA for CD163 knockout: sg2 TGAAACGCATAAACTACTTGATAAG GAAAAAGACTCAGTGGTTTACTTATTCA GTCTGCAGATAACTTCGTATAGCATACA TTATACGAAGTTATCTCAGGAAAGTATC ATGGAAACTAAATCCACACATAAACTA TGAGGAGTCTATA:	This paper	N/A

(*Continued on next page*)

Please cite this article in press as: Mauel et al., CD163+ red pulp macrophages interact with marginal metallophilic macrophages during blood-stage malaria to maintain splenic architecture, Immunity (2026), https://doi.org/10.1016/j.immuni.2026.07.006

Continued

REAGENT or RESOURCE	SOURCE	IDENTIFIER
Software and algorithms		
Fiji 2.16.0	(ImageJ distribution)	https://imagej.net/software/fiji/
GraphPad Prism v10	Dotmatics (GraphPad Software)	https://www.graphpad.com
Affinity Designer 1.10.8	Serif	https://affinity.serif.com/designer/
OMIQ (March 2025 update)	Dotmatics (OMIQ Software)	www.omiq.ai, www.dotmatics.com
Imaris x64 v9.6.1	Oxford Instruments	https://imaris.oxinst.com/
Python v3.10.16	Python Software Foundation	https://www.python.org/downloads/release/python-31016/
Scanpy v1.8.2	Wolf et al.[65]	https://scanpy.readthedocs.io/en/stable/
CellChat v2.2.0	Jin et al.[66]	https://github.com/sqjin/CellChat
gseapy v1.1.8	Fang et al.[67]	https://gseapy.readthedocs.io/en/latest/
R v4.4.2	R Foundation for Statistical Computing	https://cran.r-project.org/bin/windows/base/old/
Cell Ranger-7.1.0	10xGenomics	https://www.10xgenomics.com/support/software/cell-ranger/latest

EXPERIMENTAL MODEL AND STUDY PARTICIPANT DETAILS

Mice

All investigations concerning mouse work have local approval and all procedures conform to the guidelines from Directive 2010/63/EU of the European Parliament on protecting animals used for scientific purposes. Animal procedures were performed in adherence to the project license issued by the Landesamt für Natur, Umwelt und Verbraucherschutz (LANUV, Az.nr: 81-02.04.2020.A311, 81-02.04.2023.A144) and the University of Melbourne Animal Ethics Committees (Ethics ID 20088). Mice were maintained on a C57BL/6JRcc or C57BL/6J background and housed in specific pathogen-free conditions with 12 h light/dark cycle, with food and water provided *ad libitum*. Mice were euthanized using heart perfusion after anesthesia injection. To generate the double fate-mapper, *Tnfrsf11a*^{Cre}[68]; *Rosa26*$^{LSL\text{-}YFP}$ (JAX stock #006148)[69]; *Ms4a3*^{FlpO}[48]; *Rosa26*$^{FSF\text{-}tdTomato}$ (JAX stock #032864),[70] we bred *Tnfrsf11a*$^{Cre/+}$; *Rosa26*$^{FSF\text{-}tdTomato/FSF\text{-}tdTomato}$ animals with *Ms4a3*^{FlpO}; *Rosa26*$^{LSL\text{-}YFP/LSL\text{-}YFP}$ animals (see Figure 3A for description). For all experiments, females were analyzed. Group-housed females (and littermates of the same sex) at the age of 8-12 weeks were randomly assigned to experimental groups (control versus infection). Mice were genotyped according to protocols provided by JAX or donating researchers; primer sequences provided in Table S5. With 2 months of age, *Cxcr4*^{CreERT2} mice[14] were i.p. injected with 100 µl Tamoxifen (Sigma-Aldrich, 10 mg/ml, dissolved in 10 % Ethanol and 90 % Corn oil) for five consecutive days. *Cd163*$^{-/-}$ mice were generated with the CRISPR-Cas9 technique, depleting the sequence between intron 1 and exon 17. See key resources table for oligo sequences. Gdf15$^{-/-}$ C57BL/6 mice were generated as previously described.[64]

Plasmodium strains

The rodent malaria parasites *Plasmodium chabaudi* AS (NCBI:txid31271), *Plasmodium yoelii* NL (NCBI:txid1323249), and *Plasmodium berghei* ANKA (NCBI:txid5823) were used in this study. *P. chabaudi* AS was originally obtained from Kevin Couper (University of Manchester), *P. yoelii* NL from QIMR Berghofer Medical Research Institute (Brisbane), and *P. berghei* ANKA from the Walter and Eliza Hall Institute. Parasites were maintained as cryopreserved blood stabilates and passaged through donor mice prior to experimental infections, and parasitemia was determined by Giemsa-stained blood smears.

LCMV

Lymphocytic choriomeningitis virus (LCMV) Armstrong (species Mammarenavirus choriomeningitidis; NCBI:txid11623) was originally obtained from R. Ahmed (Emory University). Virus stocks were propagated *in vitro*, and infectious titers were determined by plaque assay and expressed as plaque-forming units.

METHOD DETAILS

Infection of experimental animals with *Plasmodium spp.* and parasitemia measurements

Donor mice were intraperitoneally (i.p.) injected with 200 µl of a frozen blood aliquot that contains 1 x 10^8 infected RBC (infection models: *P. chabaudi AS*, *P. yoelii NL*, and *P. berghei ANKA*). Parasitemia was monitored from day 5 onwards. To measure parasitemia, the tail vein was punctured with a needle (26 G) and the blood (1 - 5 µl) collected in 100 µl PBS in a 96-well plate. The DNA intercalating dye Hoechst (10 mg/ml stock) was diluted 1:1000 in PBS. An equal volume (100 µl) was added to the blood cell suspension, mixed, and incubated at 37 °C for 1 h. 200 µl FACS buffer were added and the cell suspension was filtered through a 70 µm

strainer. Samples were measured on the FACSymphony™ A5 (BD Biosciences). Mature erythrocytes have extruded their nucleus, thus only the genetic material of the intra-erythroid parasites showed Hoechst positivity. The ratio of Hoechst positive cells to all erythrocytes yielded the percentage of parasitemia. Donor mice were sacrificed when the parasitemia reached 2 - 5 % and the blood was collected. The exact parasitemia was determined and all erythrocytes counted (Neubauer chamber, 1:5000 dilution in PBS). Experimental mice were injected i.p. (for *P. chabaudi* and *P. berghei*) or i.v. (for *P. yoelii*) with a total volume of 200 µl per mouse, containing 10,000 *P. chabaudi*/*P. berghei* infected RBC or 100,000 *P.yoelii* infected RBCs from the donor mouse. The blood volume required from the donor was calculated and diluted with sterile PBS (to obtain 10,000 or 100,000 infected RBC / 200 µl). Control mice received an i.p. or i.v. injection of 200 µl of sterile PBS, respectively.

Chloroquine treatment

Mice were infected with *Plasmodium* as described above. At day 21 after the infection, the mice were i.p. injected with 200 µl of a 4 mg/ml chloroquine solution (dissolved in sterile PBS). Afterwards, mice received drinking water containing 6 mg/ml chloroquine for another 3 days.

LCMV infection

LCMV infection was performed as previously described.[71–73] LCMV Armstrong was replicated *in vitro* and the plaque forming units (PFU) were quantified to determine the viral titer. A dose of approximately 2 x 10^6 PFU was injected i.p. to develop an acute LCMV infection in C57BL/6J mice.

LPS treatment

LPS (LPS-EB Ultrapure) was dissolved in sterile PBS to obtain a concentration of 1 mg/ml. Naïve C57BL/6J mice were i.v. injected with 50 µg/kg LPS[74] or PBS as control.

Phenylhydrazine treatment

Phenylhydrazine (97 %) was prepared by diluting 100 µL of phenylhydrazine with 200 µL PEG-400 and 700 µL PBS to achieve a 100 mg/mL concentration. Subsequently, the solution was further diluted with PBS to yield 10 mg/mL. Experimental mice were injected with 40 mg/kg phenylhydrazine from the second diltuion on two consecutive days.

Preparation of cell suspension for flow cytometry

Adult mice were anesthetized and perfused with ice-cold PBS. For flow cytometry analysis of splenic myeloid cells, 25 to 35 mg of spleen was collected, cut into small pieces, and incubated in a digestion mix of PBS containing 1 mg/mL collagenase D (Roche, Cat# 11088858001), 100 U/mL DNase I (Sigma-Aldrich, Cat# DN25), 2.4 mg/ mL of dispase (Gibco Cat# 17105041) and 3% fetal calf serum (FCS) (Invitrogen) for 30 min, shaking at 700 rpm, at 37 °C before mechanical disruption through a 100 µm filter. The cell suspension was diluted in 5 ml of FACS buffer (0.5 % BSA, 2 mM EDTA in PBS) and centrifuged at 400 x *g* for 5 min. The pellet was resuspended in 1 ml red blood cell lysis buffer (155 mM NH_4Cl, 12 mM $NaHCO_3$ and 0.1 mM EDTA) and incubated for 5 min on ice. Then, 5 mL of FACS buffer was added, cells were resuspended and centrifuged at 400 x *g* for 5 min, at 4 °C. For bone marrow, one leg was isolated, and both the tibia and femur were cleaned from surrounding tissues and cut at the ends. The bones were flushed with 10 ml of ice-cold FACS buffer. Cells were centrifuged at 400 x *g* for 5 min, 4 °C and RBC-lysis was performed as described above. Blood was collected from the heart with EDTA-coated syringes in heparin-tubes. 200 µl of blood mixed with 3 ml of RBC-lysis buffer and incubated for 5 min on ice. Then, 5 mL of FACS buffer was added, cells were resuspended and centrifuged at 400 x *g* for 5 min, at 4 °C. This RBC-lysis step was repeated for the blood cell pellet. All cell pellets were resuspended in FACS buffer containing purified anti-CD16/32 and 2% rat serum (spleen and blood) or 2% rat serum only (bone marrow) and incubated for 10 min at 4 °C. Samples were immune-stained with antibody mixes for 40 min at 4 °C. Data were acquired with FACSymphony™ A5 (BD Biosciences) or Cytek™ Aurora and analyzed in FlowJo™ Software.

Unbiased clustering using OMIQ

For the unbiased clustering and visualization of splenic myeloid population, compensation, scaling, gating live, $CD45^+$, $CD11b^+$ (or $CD64^+$ cells to account for $CD11b^{low}$ cells) events, subsampling, Uniform Manifold Approximation and Projection (UMAP),[75] and FlowSOM were employed in the stated order. The analysis, along with the resultant UMAP and heatmap figures were conducted using the OMIQ software from Dotmatics (www.omiq.ai, www.dotmatics.com).

Histology

For hematoxylin-eosin (HE) staining, paraffin-embedded spleen blocks were cut at 5 µm thickness and heated for 1 h at 65 °C before staining. Sections were deparaffinized by two steps of xylol and descending series of alcohol and rinsed in distilled water. Next, sections were stained with hematoxylin solution for 1.5 min and neutralized by running tap water, followed by alcoholic eosin staining for 2 min. Sections were then dehydrated by an ascending series of alcohol and two steps of xylol and mounted with Entellan (Millipore, Cat# 1.07961.0100). Images were taken with the Axio Lab.A1 microscope. For Prussian Blue (PB) staining, paraffin-embedded spleen blocks were cut at 5 µm thickness and heated for 1 h at 65 °C. Sections were deparaffinized by two steps of xylol and descending series of alcohol and rinsed in distilled water. Next, sections were stained with potassium ferrocyanide and hydrochloric

acid for 15 min, followed by a nuclear counterstain. Sections were then dehydrated by an ascending series of alcohol and two steps of xylol and mounted with Entellan (Millipore, Cat# 1.07961.0100). For immunofluorescence staining, spleens were fixed in 4 % Formaldehyde (ThermoFisher Scientific, Cat# 11586711) for 6 hours and dehydrated overnight in 30 % D-Sucrose (ThermoFisher Scientific, Cat# 10638403) in PBS, followed by embedding in Tissue-Tek O.C.T. Compound (Sakura Finetek, Cat# 4583). Cryo-preserved spleen blocks were cut at 20 μm thickness, dried for 1 h, RT and permeabilized with PBS-T (0.4 % Triton™ X-100, Sigma-Aldrich, Cat# X100) for 3x 10 min, RT. Thereafter, tissue was blocked with PBS-T containing 5% BSA (ThermoFisher Scientific, Cat# 37525) and 2 % donkey serum (Sigma Aldrich, Cat# D9663) for 1 h, RT, followed by primary antibody staining overnight, at 4 °C. After 3x 10 min washing in PBS-T, tissue was incubated with secondary antibodies for 2 h at RT. After 3x 10 min washing in PBS-T, nuclei were stained with DAPI (Biolegend, Cat# 42281) for 5 min and slides were embedded in Fluoromount G. Immunofluorescence images were acquired with a Zeiss LSM Airyscan 710 or 880 microscope (Zeiss) and processed with Fiji.[76]

CD31+ blood-vessel proximity of splenic macrophages

The minimal distance between CD163^{high}F4/80^{+} macrophages or CD163^{-}F4/80^{+} macrophages and CD31^{+} blood vessels was quantified using Imaris x64 software (version 9.6.1). CD31^{+} vasculature was rendered as surfaces (surface detail, 0.415 μm) based on the CD31 channel, while macrophage populations were identified as spots (4.5 μm estimated XY diameter) using F4/80 and CD163 channels. Distance measurements were calculated as the shortest distance between each macrophage spot and CD31^{+} vascular surfaces. Objects intersecting image boundaries and negative distance values were excluded from analysis.

Quantification of splenic macrophage ratios

All images were processed and analyzed using ImageJ[76] (Fiji distribution, version 1.54p). For CD169^{+} MMMs, images were converted to 8-bit. Using the circular tool, outer white pulp regions were selected based on F4/80 signal. ROIs were combined using a logical XOR operation to generate a ring-shaped ROI. A threshold was uniformly applied across CD169 images (65-255) to make it binary for quantification. The Analyze Particles function (circularity 0, size 0-infinity) was then used to quantify MMMs, as an area percentage of the total marginal zone area. For CD163^{high} RPMs, as a quality control measure, images with a default threshold below 9,000 were excluded from the overall analysis. Thresholds were then uniformly applied across images to make them binary (22,000-65,535 for F4/80 and 13,000-65,535 for CD163). Double-positive CD163^{+}F4/80^{+} macrophages were identified by applying a logical AND operation to the binary masks of the CD163 and F4/80 channels to detect overlapping signal. The Analyze Particles function (circularity 0, size 0-infinity) was subsequently applied to quantify the CD163^{+} area within the F4/80^{+} macrophage population. Schematic visualization of workflow in Figures S11A and S11B.

Iron assay

Spleen homogenates were generated by mincing 8-12 mg of tissue in 200 μl ddH_2O in a 1.5 ml tube. 50 μl of Reagent A (3 g trichloroacetic acid dissolved in 3 ml H_2O, 7 ml 37% HCl added) were added. Samples were hydrolyzed by heating the tubes at 65 °C for 18 h. The solution was then vortexed and boiled for 1 h at 135 °C for total iron detection. Tubes were centrifuged (5,000 xg, 3 min, RT) to clarify the hydrolysate. 15 μl of the tissue hydrolysate were transferred into a 96-well plate (clear flat-bottom), containing 45 μl ddH_2O. Reagent B1 (15.6 g sodium acetate in 45 ml H_2O) and reagent B2 (17 mg bathophenanthroline disulfonic acid and 22 mg ascorbic acid in 5 ml H_2O) were mixed in a 9:1 ratio and 160 μl were added on top of each sample in the 96-well plate. An iron(II)-sulfate heptahydrate solution (500 μM to 7.8125 μM serial dilution) served as standard and was treated equally with reagent B. After an incubation for 10 min at RT, the absorbance was measured at 539 nm with a TECAN infinite M200 spectrometer.

CD163 ELISA

Blood was collected in heparin-coated tubes and centrifuged (1000 xg, 10 min, 4 °C). Plasma was transferred into a new tube and snap frozen. ELISA was performed according to the manufacturer's instructions (Abcam, ab272204). Samples were measured as technical duplicates.

Single-cell sequencing of enriched cells

Spleens were collected from uninfected and *P. chabaudi* infected mice at 90 dpi. Spleen cells were isolated, digested, and one fraction labeled with fluorescently-labelled antibodies (Table S7) according to the flow cytometry protocol. The homogeneous cell suspension of splenocytes was subjected to sorting with the FACS ARIA™ III cell sorter (BD Biosciences) using a 100 μm nozzle. Single, live, CD45^{+}, CD64^{+} cells were selected for sorting and collected in 100 μl FACS buffer. The other fraction was subjected to magnetic-activated cell sorting (MACS), using CD45-beads (Miltenyi, according to manufactures protocol) to retain CD45^{+} cells. The flow-through of CD45^{-} cells was collected for the sequencing protocol. To minimize transcriptional artifacts during spleen dissociation, the RNA polymerase II inhibitor flavopiridol (Sigma-Aldrich, Cat# F3055-5MG, 1 μM final concentration) was included throughout the enzymatic digestion and all subsequent processing steps.

The single-cell experiment was performed using 10x Genomics technology. Therefore, sorted cells were counted and the viability was examined by trypan blue staining using a Neubauer counting chamber. Next, the cell suspension was adjusted to a concentration of 1000 cells/μl and processed by using the 10x Genomics Chromium Controller and the Chromium Next GEM Single cell 3' Reagent Kit v3.1 (Dual Index) (PN-1000268, 10x Genomics, Pleasanton, CA, USA) according to the standard manufacturer's protocol. The loaded cells were adjusted to 16,000 cells/sample to target a recovered cell number of 10,000 cells/sample for library preparation

Please cite this article in press as: Mauel et al., CD163+ red pulp macrophages interact with marginal metallophilic macrophages during blood-stage malaria to maintain splenic architecture, Immunity (2026), https://doi.org/10.1016/j.immuni.2026.07.006

and sequencing. The cDNA integrity and concentration measurements as well as the library concentration and size distribution were assessed using an Agilent high-sensitivity D5000 assay on a Tapestation 2200 system (Agilent Technologies). The cDNA libraries were quantified using a high-sensitivity dsDNA assay (Qubit, Thermo Fisher Scientific). In the final library preparation, amplified cDNA was fragmented, and size selected using SPRIselect magnetic beads (Beckman-Coulter) to purify for a library with a size distribution of 200 - 600 bp. After adaptor ligation and sample indexing, the final fragment size and concentration were measured and samples were pooled in an equimolar range. Samples were sequenced with a sequencing depth of >30,000 reads/cell with 50 bp paired-end reads on an Illumina NextSeq2000 system. Each condition was represented by two independent biological replicates (n = 2 uninfected and n = 2 *P. chabaudi* infected), which were barcoded, processed, and sequenced in parallel to minimize technical variation.

Single-cell data alignment, read processing, data analysis, and annotation

Raw data was demultiplexed and aligned to *Mus musculus* reference genome (mm10) using Cell Ranger-7.1.0 including the intronic reads. The count matrices were processed using Scanpy (v1.8.2).[65] Low-quality cells were excluded based on the following filtering criteria: 600–8,000 genes per cell, 500–150,000 UMIs per cell, and mitochondrial gene content < 15%. Non-relevant genes (such as Malat1, mitochondrial, ribosomal, and hemoglobin genes) were removed. Doublets were identified using Scrublet[77] with a threshold of 0.22 for the doublet score. The data were normalized, log-transformed, and highly variable genes were selected for further analysis. PCA was performed, and UMAP was computed to visualize the data in two dimensions. Clusters were identified, and cell types were manually annotated based on the top 20 highly expressed genes from each cluster. Low-level carry-over of adaptive immune cells (B and T cells) into the CD64+ fraction was anticipated and handled computationally by stringent quality control, doublet removal, and marker-guided cell type annotation. Downstream macrophage-centric analyses were restricted to the relevant macrophage and monocyte subsets. Sub-clustering of the macrophage cluster was performed to identify macrophage subtypes, based on the expression of specific marker genes: *Adgre1* for RPM, *Cd209b* and *Marco* for MZM, *Cd169* for MMM, *Mertk* and *C3* for WPM.

Module score computation and statistical analysis

To quantify iron-handling macrophage identity, an RPMiron module score was computed for each cell using the score_genes function in Scanpy (v1.x), based on the method described by Tirosh et al.[78] The gene set comprised six markers associated with iron recycling and erythrophagocytosis: Cd163, Hmox1, Slc40a1, Stab2, Tfrc, and Slc11a1. For each cell, the score reflects the mean expression of the gene set relative to a randomly sampled control gene set of equal size, thereby controlling for differences in sequencing depth and gene expression variability. Analyses were restricted to RPM and RPM^{iron} subpopulations. Differences in module score between Ctrl and Malaria conditions were assessed separately for each subpopulation using a two-sided Mann-Whitney U test. P-values were corrected for multiple comparisons using the Benjamini-Hochberg false discovery rate (FDR) method. Statistical significance was defined as FDR < 0.05.

CellChat analysis

Cell-cell communication was analyzed using CellChat version 2.2.0 in R[78]. The AnnData object was converted to a count matrix for input into CellChat, and interaction networks were computed for all isolated spleen cells and subclustered macrophages. Comparisons between groups were performed using raw counts and weighted interactions. Interaction comparison plots, signaling role scatter plots, and heatmaps were generated to visualize differences in cell-cell communication. The heatmaps displayed the intensity of interactions for both raw and weighted interactions, highlighting significant communication events across spleen cells and macrophage subclusters. For the macrophage subcluster, signaling strength was calculated by evaluating both outgoing and incoming signals, and log2-fold changes between control and malaria conditions were assessed. A heatmap was generated to show upregulated and downregulated pathways in both conditions and subpopulations. Additionally, a chord diagram illustrated the changes in ligand-receptor interactions between malaria and control.

Over-representation analysis

Over-representation analysis (ORA) was performed using gseapy (version 1.1.8)[67] to identify enriched Gene Ontology (GO) terms among significantly regulated genes obtained from the single-cell RNA sequencing data. Differentially expressed genes were determined for each macrophage subset comparison (e.g., RPM^{iron} versus RPMs) using an adjusted p-value threshold of < 0.05 and an absolute $\log_2$ fold change > 0.25. Significantly up- and downregulated genes were analyzed separately. ORA was conducted with the enrich() function in gseapy using mouse-specific gene sets from the MSigDB v2024.1 Mm database, specifically the GO Biological Process collection (m5.all.v2024.1.Mm.symbols.gmt). Enrichment results were exported in tab-delimited format, and the top five significantly enriched GO terms per comparison were visualized as bar plots generated with matplotlib (version 3.10.3) in Python (version 3.10.16). The number of overlapping genes per GO term was displayed on the x-axis, and color intensity reflected the $-\log_{10}$(adjusted p-value), using cluster-specific color gradients to indicate the relative significance of the enriched pathways.

QUANTIFICATION AND STATISTICAL ANALYSIS

Statistical tests were carried out with GraphPad Prism 10 (GraphPad Software Inc.) and Python (v3.10.16). All data-sets were tested for outlier (ROUT, Q = 1 %). Normal distribution of data was tested with Shapiro-Wilk normality test (significance level (alpha) = 0.05).

Please cite this article in press as: Mauel et al., CD163^{+} red pulp macrophages interact with marginal metallophilic macrophages during blood-stage malaria to maintain splenic architecture, Immunity (2026), https://doi.org/10.1016/j.immuni.2026.07.006

For normally distrusted data, One-way ANOVA with multiple comparisons (Bonferroni correction) or the unpaired Student's t-test with Welch's correction was performed. For not normally distributed data sets, Kruskal-Wallis test was performed (with Dunn's multiple comparison test) or Mann-Whitney test when non-parametric. R version 4.4.2 and Prism were used for the statistical evaluation and visualization. Data are shown as mean ± SD. Statistical significance was represented via the probability (p-value) as follows: * = $p<0.05$, ** = $p<0.01$, *** = $p<0.001$, **** = $p<0.0001$. Data are shown as mean ± SD. Numbers of biological and technical replicates are specified in figure legends. Confocal images were visualized and analyzed using Fiji and IMARIS. Specific thresholds and cutoffs used for analysis of scRNA-seq data are described in detail in the relevant method details section.